QuickCSG: Arbitrary and Faster Boolean Combinations of N Solids

Matthijs Douze, Jean-Sébastien Franco, Bruno Raffin

QuickCSG: Arbitrary and Faster Boolean Combinations of N Solids

Matthijs Douze, Jean-Sébastien Franco, Bruno Raffin

RESEARCH REPORT

N° 8687

March 2015

Project-Teams Morpheo, Moais

ISSN 0249-6399 ISRN INRIA/RR--8687--FR+ENG

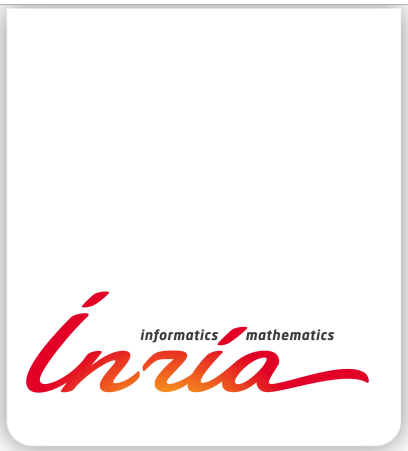

QuickCSG: Arbitrary and Faster Boolean Combinations of N Solids

Matthijs Douze, Jean-Sébastien Franco, Bruno Raffin

Project-Teams Morpheo, Moais

Research Report n° 8687 — March 2015 — 36 pages

Abstract: While studied over several decades, the computation of boolean operations on polyhedra is almost always addressed by focusing on the case of two polyhedra. For multiple input polyhedra and an arbitrary boolean operation to be applied, the operation is decomposed over a binary CSG tree, each node being processed separately in quasilinear time. For large trees, this is both error prone due to intermediate geometry and error accumulation, and inefficient because each node yields a specific overhead. We introduce a fundamentally new approach to polyhedral CSG evaluation, addressing the general N-polyhedron case. We propose a new vertex-centric view of the problem, which both simplifies the algorithm computing resulting geometric contributions, and vastly facilitates its spatial decomposition. We then embed the entire problem in a single KD-tree, specifically geared toward the final result by early pruning of any region of space not contributing to the final surface. This not only improves the robustness of the approach, it also gives it a fundamental speed advantage, with an output complexity depending on the output mesh size instead of the input size as with usual approaches. Complemented with a task-stealing parallelization, the algorithm achieves breakthrough performance, one to two orders of magnitude speedups with respect to state-of-the-art CPU algorithms, on boolean operations over two to several dozen polyhedra. The algorithm is also shown to outperform recent GPU implementations and approximate discretizations, while producing an exact output without redundant facets.

Key-words: CSG, Polyhedra, boolean operations

This is a note

This is a second note

RESEARCH CENTRE
GRENOBLE – RHÔNE-ALPES

Inovallée
655 avenue de l'Europe Montbonnot
38334 Saint Ismier Cedex

QuickCSG: combinaison booléenne arbitraire et rapide de N solides

Résumé : Quoique étudié depuis des décennies, le calcul d'opérations booléennes sur des polyèdres est quasiment toujours fait sur deux opérandes. Pour un plus grand nombre de polyèdres et une opération booléenne arbitraire à effectuer, l'opération est décomposée sur un arbre binaire CSG (géométrie constructive), dans lequel chaque nœud est traité séparément en temps quasi-linéaire. Pour de grands arbres, ceci est à la fois source d'erreurs, à cause des calculs géométriques intermédiaires, et inefficace à cause des traitements superflus au niveau des nœuds. Nous introduisons une approche fondamentalement nouvelle qui traite le cas général de N polyèdres. Nous proposons une vue du problème centrée sur les sommets, ce qui simplifie l'algorithme et facilite sa décomposition spatiale. Nous traitons le problème dans un seul KD-tree, qui est dirigé vers le résultat final, en élaguant les régions de l'espace qui ne contribuent pas à la surface finale. Non seulement ceci améliore la robustesse de l'approche mais ça lui donne un avantage en vitesse, car la complexité dépend plus de la taille de la sortie que celle d'entrée. En la combinant avec une parallélisation basée sur du vol de tâche, l'algorithme a des performances inouïes, d'un ou deux ordres de grandeur plus rapide que les algorithmes de l'état de l'art sur CPU et GPU. De plus il produit un résultat exact, sans aucune primitive géométrique superflue.

Mots-clés : Opérations booléennes, polyèdres

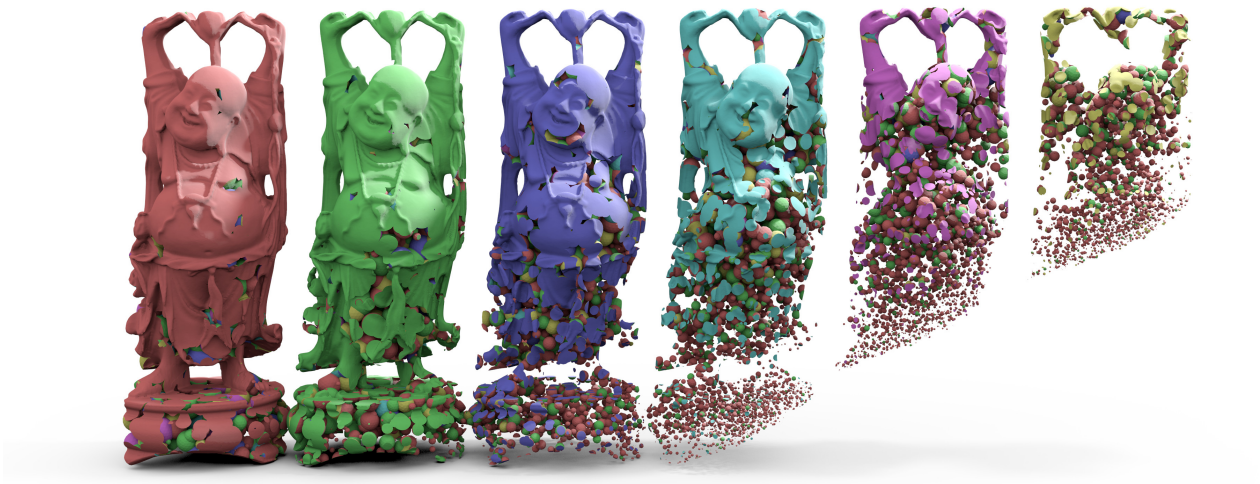

Figure 1: Intersection of 6 Buddhas with the union of 100,000 spheres (total 24 million triangles). Computed in 8 seconds on a desktop machine.

1 Introduction

Solid modeling using boolean operations is an emblematic problem in computer graphics and computational geometry, almost as old as these research topics themselves. It has found its way in every solid modeler in the industry, whether applied to model design for aviation, transportation, manufacturing, architecture, or entertainment. It is also an ubiquitous building block and subject of interest for many fields of research, including computer graphics, computer vision, robotics, virtual reality, and generally any topic where geometric models of subjects of interest are to be manipulated, constructed, truncated or combined.

Since the first introduction of boundary representations (B-Rep) [Baumgart, 1974], the problem has received considerable attention and been the subject of extensive work over more than 40 years. It is all the more striking that, despite the many existing algorithms and variants in this huge corpus, the vast majority of algorithms generally rely on a common principle and canvas found in the earliest formalizations of the problem [Requicha and Voelcker, 1985, Laidlaw et al., 1986]. First and foremost, boolean B-Rep merging algorithms are most often written for the case of two solids. Second, the computation is most commonly divided in three stages: an initial *subdivision* stage, where the boundaries of both objects are split in two component groups along their intersection with the other object's boundary. A *classification* stage follows, where each group is classified as belonging inside or outside the other object. In the final *reconstruction* stage, the relevant primitives are gathered and connected to build the final model in accordance to the boolean expression. Note that the subdivision and classification require to intersect and situate all primitives of an object's boundary with respect to the primitives of the other object's boundary, which if done naively leads to impractical quadratic-time algorithms. Thus, a third common aspect of most algorithms is the use of spatial decomposition structures, often hierarchical, to enable sublinear $\mathcal{O}(\log n)$ access to each object's primitives. The construction of this data structure usually becomes the bottleneck of the algorithm, giving it its typically quasi-linear time complexity $\mathcal{O}(n \log^d n)$ in the number of input primitives [Hachenberger et al., 2007] (where d is a constant).

In a majority of the use cases, solids are built using several different input shapes with a com-

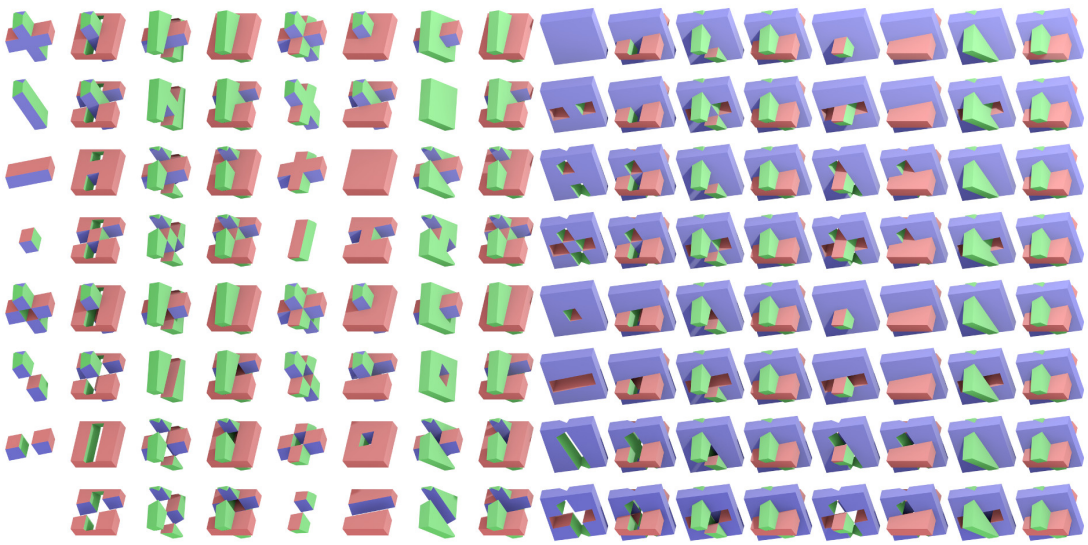

Figure 2: There are 256 possible boolean operations between three polyhedra, of which we show 128, applied to 3D boxes (the 128 other ones are the same with inside and outside flipped). Like on all images of the paper, each input polyhedron is assigned a color, and the output facets inherit the color of the input mesh they came from.

plex combination. This has been formalized as Constructive Solid Geometry (CSG) [Requicha, 1980, Mäntylä, 1987] where a solid is defined by a tree of boolean operations from a set of primitive solids. In fact, it can be applied to any B-Rep solid, provided each node of the tree be evaluated with a B-Rep boolean operator. Note that union and intersection operations need not be limited to two operands. This begs for the question, why not examine the entire problem at once and only compute the final result? By focusing on the final boundary only, less time is spent on computing intermediate results which, for most purposes, will be discarded anyway, and may additionally introduce uncertainty accumulation and computation errors in successive and inter-dependent computations. We propose a new algorithm based on this intuition, and validate it theoretically and experimentally.

Contributions. In this paper, we challenge the dominant view of boolean modeling, by allowing arbitrary sets of input solids to be combined using arbitrary boolean expressions. This formalism not only leads to a very simple algorithm, it also opens new possibilities to easily formulate boolean expressions on solid sets as general bit vector operators, which would otherwise be inconvenient or impossible to express using a classical binary boolean tree. A simple example of such an expression is the polyhedron that contains the regions in space where at least k out of n input polyhedra intersect: the boolean tree of this expression is of combinatorial size in n and k. In our formalism, this translates to counting bit contributions in an occupancy bit vector for each final candidate vertex. Figure 2 shows all three-input boolean expressions. As another defining choice, our algorithm performs the classification and subdivision stages simultaneously, by embedding all input solids in a single KD-tree structure. The algorithm seeks to classify each node of the KD-tree as soon as it is created, by inferring whether its contents is completely inside or outside the final solid, or if it may participate to the final solid boundary instead. The KD-tree is only subdivided in the latter case, pruning large sets of primitives that do not

need additional work, and focusing all computational effort and refinement on those space cells containing intersecting primitives participating to the final result. As a result, the depth and size of our KD-tree no longer depends on the size of the inputs but on the size of the output model, leading to gains in time and space complexity that grow with the number of input solids and the input-to-output primitive ratio. This in particular means that our algorithm also outperforms the traditional two-solid boolean algorithms as soon as the result size is smaller than the input size. Finally, as our KD-tree decomposes space into non-intersecting cells that can be processed independently, the classification stage and subsequent subdivision and reconstruction stages naturally lend themselves to parallel evaluation, further substantiating the temporal gain over all state-of-the-art polyhedral boolean evaluation algorithms tested, including recent GPU implementations.

1.1 Boolean Solid Modelling Background

In the 1970's, boolean solid modeling and boundary representations (B-Reps) have been simultaneously pioneered in the context of computer graphics [Braid, 1975] and computer vision [Baumgart, 1974]. Both proposed discrete representations of solid boundaries as a conjunction of simpler polygonal primitives, either winged edges (Baumgart) or loops (Braid). While many of the ideas are already present in Braid's work, the idea that solids could be specified as a tree of boolean operations (Constructive Solid Geometry or CSG) was theorized by [Requicha, 1980], and various practical implementations proposed for polyhedral boundaries [Requicha and Voelcker, 1985, Laidlaw et al., 1986], in particular setting the standard for the aforementioned 3-stage algorithm. Robustness was by then identified as a recurring issue, due to lack of formal description of degenerate solid configurations, and numerical computation error in near-coincident situations. Most algorithms thereafter, including industrial implementations, thus conform to a set-based formalism with algebraically closed regularized boolean set operations [Requicha, 1977], ensuring results exclude any non-volume enclosing (dangling) surface primitives. Several works also took on the task of painstakingly accounting for all degenerate relative configurations of solid primitives [Hoffmann, 1989, Mäntylä, 1987], leading to tedious algorithm descriptions. They notably formalize the B-Rep primitive hierarchy as vertex, edges, faces and shells, and the two-polyhedra intersections and degeneracy cases as arising from the possible intersection combination of each primitive type of solid A to each primitive type of solid B. To avoid the complete enumeration, many implementations focus on generic triangle-to-triangle or polygon-to-polygon as their central intersection unit. Even with this simplification, the complexity of dealing with all cases is known to yield unreliable implementations, including in commercial software, as reported in various test cases [Wang, 2011, Feito et al., 2013]. Our algorithm has a significantly simplified core that focuses all classification and subdivision efforts on producing the final output vertices, excluding higher order primitives or intermediate vertices. The final reconstruction stage thus mainly operates on these vertices, identifying the topologically correct final edges and loops through a posteriori logical vertex-to-vertex reconnections. This both drastically improves the clarity and regularity of the proposed algorithm, and paves the way for tackling the otherwise unaffordable exact topology retrieval in the general N-polyhedron case.

Robustness has remained a dominant issue, with various solutions proposed reviewed by e.g. [Hoffmann, 2001, Li et al., 2004], such as geometric predicate analysis and fixed or arbitrary precision exact arithmetics. This effort has culminated with Hachenberger's work on CGAL [Hachenberger et al., 2007], which uses arbitrary precision arithmetic, with the particularity that it follows Nef's formalism [Nef, 1978] instead of regularized booleans [Requicha, 1977], i.e. it explicitly represents dangling primitives. While now standing out as a reference imple-

mentation of the research community, it is notoriously slow, and as most exact schemes, tedious to re-implement, leading to a somewhat paradoxical status: while the perception of the community is that the polyhedral B-Rep boolean problem is solved, free and commercial code is still being crafted and distributed using fragile but fast and memory-efficient geometric predicate evaluations.

Most new contributions in this area are focusing on speeding up or easing the implementation of various algorithmic work cases of the classic two-polyhedron boolean algorithms, with e.g. new specialized data structures [Campen and Kobbelt, 2010], faster exact arithmetic types [Bernstein and Fussell, 200 or optimization for particular inputs such as triangular meshes [Feito et al., 2013] or polyhedral cones of arbitrary basis [Franco and Boyer, 2009]. Each implementation relies on specific and non-optimal tradeoffs between implementation complexity, speed, memory footprint, input genericity, robustness (or lack thereof). We simultaneously improve over all problematic aspects: our greedy pruning scheme eliminates the need to compute any intermediate geometry and thus improves the complexity, robustness, memory footprint and execution time while enabling multiarity boolean operations on N polyhedra, including but not limited to binary boolean trees. As this result strongly relies on the careful use of hierarchical subdivision structures, we will specifically review this aspect of prior art in the following section.

1.2 Subdivision Structures for Efficient Computation

Because of the need for efficient subdivision and classification stages in the algorithm, a substantial research effort has been devoted to hierarchical structures in the context of boolean solid modelling. Some of the earliest axis-aligned plane-separation structures in this context are the polytrees [Carlbom, 1987] and extended octrees, which embed the polyhedral B-Rep primitives in their nodes [Brunet and Navazo, 1990]. Binary space partitions (BSP) of polyhedral B-Reps were devised as a way to more efficiently store the polyhedron as the tree separating planes themselves [Thibault and Naylor, 1987]. The most common strategy to compute boolean combinations of two solids with these representations is to perform simultaneous traversal of both hierarchies to isolate intersecting primitives [Brunet and Navazo, 1990], or similarly compute a merged BSP tree itself representing the result [Naylor et al., 1990]. Recent reference implementations continue to use variants of these seminal approaches, e.g. CGAL uses KD-trees as accelerated axis-aligned plane separating search structures [Hachenberger et al., 2007], GTS uses axis-aligned bounding box (AABB) trees [Popinet, 2006], while Carve CSG uses octrees [Sargeant, 2011]. A number of hybrid variants exist, which seek simultaneous benefit from the access simplicity of the octree structure and the representational flexibility of BSPs [Adams and Dutré, 2003].

Of significant interest among such hybrid methods, [Pavic et al., 2010] have begun to leverage the idea that better performance could be achieved by examining the boolean CSG binary tree with a single octree embedding all input geometry, subdividing cells down to a fixed cell size as long as two input solids are volumetrically present, then classifying each leaf cell after subdivision by evaluating the CSG boolean tree expression. A key difference with our proposal, is that the resulting meshes are stitched with an approximate local triangulation at intersecting leaf cells, while we compute true surface-to-surface boolean contributions, for arbitrary boolean expressions that need not be expressed with a boolean tree. [Feito et al., 2013] uses a similar octree subdivision triggered by general two-surface presence, but focuses only on triangular meshes and the two-solid case. Fundamentally for both approaches it can be noted that, similarly to other existing approaches previously mentioned, classification is still independently computed and not used to guide the subdivision.

A compelling case we make in this paper is that separating subdivision and classification stages, as done to date by all boolean B-Rep algorithms we are aware of, leads to an inherently

suboptimal boolean algorithm. In light of the review of prior art, this is because the hierarchical structures proposed are in the vast majority of cases constructed as alternate representations of *each individual input solid*, decomposing its inherent geometric details with trees of logarithmic depth in that input solid's size. In contrast, our algorithm builds a single geometric decomposition, splitting nodes according to a partial classification of their content computed on the fly. Branches not contributing to the resulting solid are pruned away, yielding a tree whose nodes are focused on the final surface geometry, with a depth logarithmic in the number of intersections present in the *resulting solid* instead. This yields two fundamental improvements over state of the art. First the algorithmic complexity is improved as it now proportional to the logarithm of the resulting solid size. Second, because this tree classifies final contributions on the fly during subdivision, our algorithm does not need to store the full tree in memory, only the information of the currently explored tree branch. This frees the algorithm from storing the subdivisions structures of each input solid in preparation for a separate classification stage, as with previous methods.

2 N-Polyhedron CSG Formalization

This section introduces the representation of the input solids and the CSG operation.

2.1 Definitions

We consider n input polyhedra $\{\mathcal{P}_i\}_{i\in\{1,\cdots,n\}}$, whose surfaces are assumed to be closed orientable 2-manifolds embedded in $\mathbb{R}^3$, *i.e.* surfaces with no holes and with a consistent normal orientation. These classical assumptions ensure every polyhedron non-ambiguously defines a closed volume of $\mathbb{R}^3$. Each input polyhedron $\mathcal{P}_i = (\mathcal{V}_i, \mathcal{F}_i)$ is defined by its set of vertices $\mathcal{V}_i$ and facets $\mathcal{F}_i$, each described as a loop of vertex indices whose order is consistent, *e.g.* typically given with counterclockwise orientation as seen from its outer region. We assume unicity of vertices, *i.e.* no vertex coordinates are duplicated and adjacent loops share common vertices. A polyhedron may have various connected components. Facets are assumed convex and described with a single loop to simplify the explanation and implementation, although the reasoning extends to general, non-convex polygons with several components.

The resulting shape may be complex, as any output facet may potentially be shaped by arbitrary primitives of all inputs. The complexity of possible degeneracies between all types of primitives for two-polyhedron booleans is already quite daunting and error-prone to implement [Hoffmann, 1989]. Generalizing Hoffmann's analysis to n-case degeneracies is not desirable nor practical. As an example, degenerate output vertices may arise from the coincidental positioning of anywhere from 4 to n input facets chosen among any input solid's facets, all of which would result in different special cases for reconstructing the vertex neighborhood. Add to this the various degeneracy possibilities for multiple coincidental vertices, edges, facets, or any combination thereof, and the number of special cases to deal with is unpredictably large to enumerate. Fortunately, [Edelsbrunner and Mücke, 1990] have shown that *describing the non-degenerate cases of geometric algorithms is entirely sufficient*, a key assumption we shall build our framework on. In their work, degeneracies are handled by introducing tie-breaking rules based on symbolic perturbations of input primitives. In practice, implementations most often get away with using double-precision floating-point arithmetic, as degeneracy cases are shown to be highly unlikely when dealing with noisy inputs, either resulting from an acquisition process [Curless and Levoy, 1996, Franco and Boyer, 2009] or artificially generated with jittering for this purpose.

2.2 Boolean Functions of n inputs

Instead of the usual CSG tree form of boolean expressions, we provide a framework for arbitrary expressions. We express a boolean solid operation using a boolean-valued function over n boolean inputs, $f : \{0,1\}^n \to \{0,1\}$. We note $\mathbb{I}_i(x) \in \{0,1\}$ the indicator function of polyhedron $\mathcal{P}_i$, whose value reflects whether a point $x \in \mathbb{R}^3$ is in polyhedron $\mathcal{P}_i$'s inner volume. The indicator function $\mathbb{I}_f(x)$ of the final solid $\mathcal{P}_f$ can then be computed using f:

$$\mathbb{I}_f(x) = f(\mathbb{I}_1(x), \cdots, \mathbb{I}_n(x)). \tag{1}$$

We define the *indicator vector* of point x as the tuple of its n indicator functions, $\mathbf{I}(x) = (\mathbb{I}_1(x), \cdots, \mathbb{I}_n(x))$, and sometimes denote the CSG operation as occurring over its indicator vector, *i.e.* $\mathbb{I}_f(x) = f(\mathbf{I}(x))$. Note that, as $\mathcal{P}_i$ is given as a set of vertices and faces $(\mathcal{V}_i, \mathcal{F}_i)$, indicator function values $\mathbb{I}_i(x)$ are to be computed based on the Jordan curve theorem [Agoston, 2005], by shooting a ray and computing the winding numbers of x [Schneider and Eberly, 2003]. If a vertex is known to belong to the surface of a polyhedron, we denote the corresponding boolean value as 's' (see Figure 3). Note that we never compute function f on s inputs.

Any indicator function $\mathbb{I}_f(x)$ can be evalued from classical binary boolean operators (eg. as a conjunction of disjunctions), but alternative evaluations are also possible based on, for instance, higher arity boolean operators or arithmetic operations. The rationale is to simplify the expression of some operations and speed up the evaluation. The following examples show a few operators whose n-ary formulation enables efficient evaluations:

$$\text{n-Intersection:} \quad \mathbb{I}_\cap(x) = \min(\mathbb{I}_1(x), \cdots, \mathbb{I}_n(x)), \tag{2}$$

$$\text{n-Union:} \quad \mathbb{I}_\cup(x) = \max(\mathbb{I}_1(x), \cdots, \mathbb{I}_n(x)), \tag{3}$$

$$\text{Mutual exclusion:} \quad \mathbb{I}_{\text{xor}}(x) = \mathbb{I}_1(x) \,\text{xor}\, \cdots \,\text{xor}\, \mathbb{I}_n(x), \tag{4}$$

$$\text{In } k \text{ or more solids:} \quad \mathbb{I}_{\text{min-}k}(x) = (\textstyle\sum_i \mathbb{I}_i(x)) \geq k. \tag{5}$$

The min-k and operation retrieves the solid being part of at least k input polyhedrons. This operation in particular would be tedious to decompose over a binary CSG tree: it requires to evaluate the union of all possible intersections of $n - k$ solids, leading to a tree of combinatorial size.

Since the indicator vector can be efficiently represented as a bit vector stored in machine words, evaluating typical boolean functions f is for most practical purposes a constant time operation in n, either by directly evaluating a boolean test expression over the machine word, or by building lookup/hash tables for compatible expressions. Any binary tree of CSG operations can be expressed as a single boolean function. Therefore, models built by binary CSG operations can be constructed in one pass by our algorithm. We will see below how these definitions will be used to make final boundary surface decisions.

3 Final Polyhedron Vertices

We now analyze the structure of the final polyhedron $\mathcal{P}_f$, focusing on its vertices. With primitives in generic (*i.e.* non coincidental) position as assumed, vertices of the final polyhedron can be of only three types (Figure 3):

- *First order vertices* are vertices already present in one of the input polyhedra $\mathcal{P}_i$'s vertex set $\mathcal{V}_i$.

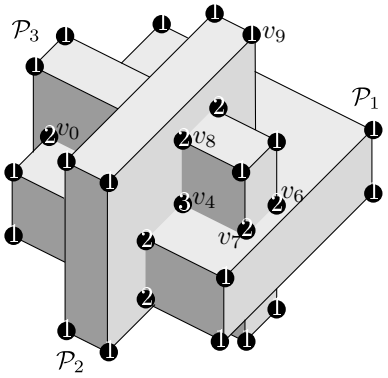

vertex	indicator
v_0	$(s, 0, s)$
v_4	(s, s, s)
v_6	$(s, 0, s)$
v_7	$(s, 0, s)$
v_8	$(0, s, s)$
v_9	$(0, s, 0)$

Figure 3: Combination of three solids, with the orders of the vertices (in black circles). Left: the indicator vector for some of the vertices.

- *Second order vertices* result from the intersection of an edge of a polyhedron $\mathcal{P}_i$ and the facet of another polyhedron $\mathcal{P}_j$.
- *Third order vertices* result from the intersection of three facets of three different polyhedra $\mathcal{P}_i$, $\mathcal{P}_j$, and $\mathcal{P}_k$.

A trivial way to generate all possible vertex candidates is thus to examine all possible input vertices, edge-to-facet combinations, and three-facet combinations, and compute the resulting geometric intersections, using standard algorithms for these cases [Schneider and Eberly, 2003]. Input primitives may intersect at various locations in space, without necessarily participating to the final surface, as determined by the CSG function. We propose a classification process to select the candidates vertices participating to the output result. Our description is illustrated on the left column of Fig. 4, which summarizes the geometry of vertices of each possible order, and the notations used. In this figure, orientation information is given in red, and classification information in green. In particular, small green grids are given to break down complex local subvolume configurations around the vertex v, and their corresponding classification bits, which determine their inclusion inside the final volume of $\mathcal{P}_f$ and are hereunder defined.

3.1 Vertex Classification

Intuitively a necessary condition for a vertex candidate to be kept is for it to lay at the border of the final solid, in other words it should be part of a surface transition from inside to outside $\mathcal{P}_f$. But this condition is not sufficient as we will see.

The condition is sufficient for a **first order vertex.** By definition, the candidate vertex v participates in the boundary of one input polyhedron $\mathcal{P}_i$, which separates the vicinity of the vertex into two subvolumes, inside and outside $\mathcal{P}_i$. For this vertex to lay on the boundary of $\mathcal{P}_f$, it must also partition the surrounding volume into inside and outside regions of $\mathcal{P}_f$. This information can be obtained by examining how $f(\mathbf{I}(v))$ transitions at the boundary of $\mathcal{P}_i$, *i.e.* when the i-th bit of the indicator vector, initially a s bit, is flipped between 0 and 1:

$$f(\mathbb{I}_1(v), \cdots, 0, \cdots, \mathbb{I}_n(v)) \neq f(\mathbb{I}_1(v), \cdots, 1, \cdots, \mathbb{I}_n(v)). \tag{6}$$

This conditions is noted `isFinal1`(v), and tests wether there is a final indicator change when the boundary of $\mathcal{P}_i$ is traversed. If the two expressions were equal, then the vertex v would be

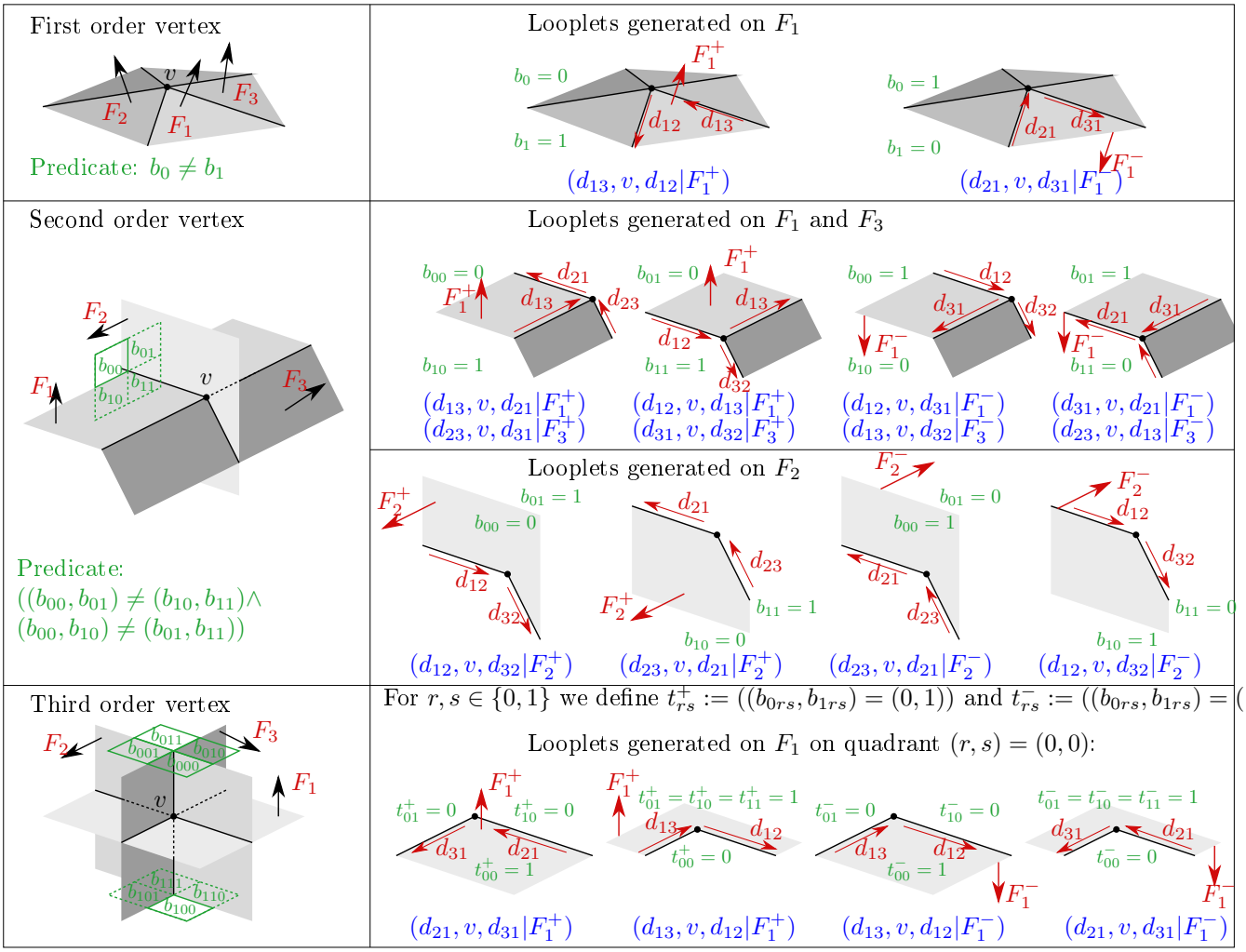

Figure 4: Vertex configurations and their corresponding possible looplets.

completely inside (both 1) or outside (both 0) $\mathcal{P}_f$. This assumes all other bits $\mathbb{I}_j(v)$, with $j \neq i$, were computed for vertex v by *e.g.* ray shooting.

Second order vertex. Because facets of two polyhedra $\mathcal{P}_i$ and $\mathcal{P}_j$ are involved, the volume surrounding the vertex candidate is locally partitioned in four subvolumes, each of which may be decided to be inside or outside the final polyhedron $\mathcal{P}_f$ by the CSG function f. We must therefore examine how each combination of boundary traversals at vertex v influence the final indicator function, by evaluating the corresponding i and j bit-flippings of $\mathbf{I}(v)$:

$$\begin{array}{ll} b_{00} & = f(\mathbb{I}_1(v), \cdots, 0, \cdots, 0, \cdots, \mathbb{I}_n(v)) \\ b_{01} & = f(\mathbb{I}_1(v), \cdots, 0, \cdots, 1, \cdots, \mathbb{I}_n(v)) \\ b_{10} & = f(\mathbb{I}_1(v), \cdots, 1, \cdots, 0, \cdots, \mathbb{I}_n(v)) \\ b_{11} & = f(\mathbb{I}_1(v), \cdots, 1, \cdots, 1, \cdots, \mathbb{I}_n(v)). \end{array} \tag{7}$$

We call $\mathbf{b}(v) = (b_{00}, b_{01}, b_{10}, b_{11}) \in \{0,1\}^4$ the classification vector of second order vertex v. Trivially, if all four bits turn out equal, the vertex v is either completely inside (all 1's) or outside (all 0's) of $\mathcal{P}_f$ and does not participate to the final surface. In the general case, vertex candidates may lay on the final boundary and still not participate to the final surface description. This is the case if the introduction of this vertex does not change the final geometry, *i.e.* if the vertex is introduced in the middle of a final planar polygon of a final edge. This happens as soon as the bit pattern of v is symmetric along one of the components i or j, because this means that traversing the vertex along this border leaves the final primitive participation of the other involved polyhedron completely unchanged. A sufficient condition can thus be written as the predicate `isFinal2`(v), which rules out any topological symmetries along the i or j components, as underlined in subscripts:

$$\left((b_{\underline{00}}, b_{\underline{01}}) \neq (b_{\underline{10}}, b_{\underline{11}})\right) \wedge \left((b_{\underline{00}}, b_{\underline{10}}) \neq (b_{\underline{01}}, b_{\underline{11}})\right) \tag{8}$$

It can be noted that this condition includes the necessary conditions, since complete inclusion or exclusion is also a case of pattern symmetry. Enforcing pattern asymmetry also imposes the existence of final indicator changes for all boundary transitions, ensuring that the vertex lays on the final boundary surface of $\mathcal{P}_f$.

Third order vertex. At the intersection locus of three facets from three input polyhedra $\mathcal{P}_i$, $\mathcal{P}_j$, $\mathcal{P}_k$, the vertex's neighborhood is locally split in eight subvolumes. The analysis is analog to second order vertices, and requires examining the influence of crossing the three boundaries. The corresponding 8 combinations of i, j and k bit-flippings are:

$$\begin{array}{ll} b_{000} & = f(\mathbb{I}_1(v), \cdots, 0, \cdots, 0, \cdots, 0, \cdots, \mathbb{I}_n(v)) \\ b_{001} & = f(\mathbb{I}_1(v), \cdots, 0, \cdots, 0, \cdots, 1, \cdots, \mathbb{I}_n(v)) \\ & \cdots \\ b_{111} & = f(\mathbb{I}_1(v), \cdots, 1, \cdots, 1, \cdots, 1, \cdots, \mathbb{I}_n(v)). \end{array} \tag{9}$$

We call $\mathbf{b}(v) = (b_{000}, \cdots, b_{111}) \in \{0,1\}^8$ the classification vector of third order vertex v. Similarly to the order 2 case, complete inclusion or exclusion of the volume rules out the vertex, as well as any axis symmetries, which can be jointly evaluated with the predicate `isFinal3`(v):

$$\begin{array}{ll} & \left((b_{\underline{000}}, b_{\underline{001}}, b_{\underline{010}}, b_{\underline{011}}) \neq (b_{\underline{100}}, b_{\underline{101}}, b_{\underline{110}}, b_{\underline{111}})\right) \\ \wedge & \left((b_{\underline{000}}, b_{\underline{001}}, b_{\underline{100}}, b_{\underline{101}}) \neq (b_{\underline{010}}, b_{\underline{011}}, b_{\underline{110}}, b_{\underline{111}})\right) \\ \wedge & \left((b_{\underline{000}}, b_{\underline{010}}, b_{\underline{100}}, b_{\underline{110}}) \neq (b_{\underline{001}}, b_{\underline{011}}, b_{\underline{101}}, b_{\underline{111}})\right) \end{array} \tag{10}$$

If none of these conditions are met, the vertex is completely inside or outside the result polyhedron. If one (resp. two) of the conditions are met, the vertex is on a facet (resp. edge) of the final polyhedron.

Specificity of the 2-polyhedron case. Interestingly, in this situation, there are only first and second order vertices with no axis symmetries, *i.e.* all order two vertex candidates participate to $\mathcal{P}_f$ [Franco et al., 2013].

3.2 Vertex Retrieval Summary

We illustrate in Fig. 5 how a set of vertices may be retrieved using a cubic complexity algorithm which loops over all face combinations, using the previously defined isFinal1, isFinal2, and isFinal3 predicates. It uses classical intersection functions [Schneider and Eberly, 2003]: intersect2facets computes the intersected edge between two convex facets, as a pair of vertices giving the edge extremities, and intersectSegmentFacet computes the vertex representing the intersection of a segment and a facet, if any.

```
function CSGVertices
    Input: 𝒱, ℱ: set of vertices and facets of input polyhedra
    Output: 𝒱_f: corresponding set of final output vertices
    for F_1 in ℱ do                                          ▷ Enumerate input faces
        for v in F_1 do                                      ▷ Order 1 candidates
            if isFinal1(v) then 𝒱_f := 𝒱_f ∪ v
        end for
        for F_2 in ℱ do
            v_1, v_2 := intersect2facets(F_1, F_2)           ▷ Order 2 candidates
            if {v_1, v_2} = ∅ then continue F_2 loop         ▷ No intersection
            if isFinal2(v_1) then 𝒱_f := 𝒱_f ∪ v_1
            if isFinal2(v_2) then 𝒱_f := 𝒱_f ∪ v_2
            for F_3 in ℱ do                                  ▷ Order 3 candidates
                v := intersectSegmentFacet(v_1, v_2, F_3)
                if v ≠ ∅ and isFinal3(v) then 𝒱_f := 𝒱_f ∪ v
            end for
        end for
    end for
end function
```

Figure 5: Brute-force algorithm to find all vertices of the result polyhedron.

4 Final Polyhedron Connectivity

Once the subset of final vertices $\mathcal{V}_f$ is known through the classification process, the main task left is to identify how vertices are connected together to form the faces $\mathcal{F}_f$ of the final polyhedron $\mathcal{P}_f$. Our method makes a clear distinction between computing all geometric coordinates of final vertices and building the final topology. While the former involves numerical coordinate construction, the latter relies only on orientation and ordering predicates.

The classification vectors previously introduced not only inform us of the participation of a given vertex v to $\mathcal{P}_f$, they also give a full snapshot of volume and surface adjacencies around the vertex, as illustrated in Fig. 4. We show here how to find all the polygons v participates in, with the introduction of the *looplet* construct. We define a looplet of v as a loop fragment running through this vertex, represented by an incoming and outgoing edge direction. The looplet serves the following purposes:

- Many different edge adjacencies are possible along the planes coincident at the vertex, but only a subset end up being used for a given vertex v. The classification vector of v determines in which particular directions such vertex adjacencies exist.
- Representing incoming and outgoing directions in a looplet explicitly identifies in which plane and final facet the vertex participates in, and is thus more informative than looking at each direction alone.
- Once the looplets are generated for all final vertices in $\mathcal{V}_f$, it identifies final facets of $\mathcal{F}_f$, is a matter of chaining looplets of each final facet plane. This boils down to identifying vertex pairs that admit coinciding incoming and outgoing edge directions in the face.

4.1 Surface and Edge Orientation

A proper identification of surface and edge orientation is necessary to define looplets. Surface boundaries contributing to the final result $\mathcal{P}_f$ may change orientation, *e.g.* when participating in a boolean subtraction. For any facet F_a of any polyhedron, we note the orientation of its contributions to the final surface as either F_a^+ if the contribution conserves initial orientation, and F_a^- if the orientation of the contribution is inverted. In similar spirit we need to define an intrinsic edge orientation d_{ab} for every edge adjacent to two faces F_a and F_b. For this purpose we distinguish two cases:

- if the edge is pre-existing from an input $\mathcal{P}_i$, d_{ab} is the edge direction with polygon F_a on its left and F_b on its right on the oriented surface.
- if the edge arises from the intersection of F_a and F_b, we define the edge direction $d_{ab} = F_a \times F_b$, as the crossproduct of the corresponding face normals.

Note that in both cases $d_{ab} = -d_{ba}$. With these definitions we can introduce a concise notation for looplets, as $(d_{ab}, v, d_{ac}|F_a^+)$, a looplet characterized as a positive contribution in F_a, centered on vertex v, with incoming edge direction d_{ab} and outward edge direction d_{ac}. In the following, we will describe how knowledge of the classification vectors directly determines which looplets are present at a vertex, upon which the final polyhedron facets can be built. For this purpose, we break down the presentation of looplet generation cases for each vertex order. This breakdown is illustrated in the right column of Fig. 4, where each subfigure shows in green the bit classification state deciding the presence of corresponding looplets, annotated under the figure in blue.

4.2 First Order Vertex Looplets

A first order vertex v that passed the classification test is on the polyhedral boundary of a polyhedron $\mathcal{P}_i$ that is also part of the final polyhedron's boundary. Each of its immediately adjacent facets thus at least partially participates to $\mathcal{P}_f$, and contributes a looplet for this vertex. The directions of this looplet are given by the edges adjacent to the facets of the looplet. If there is no change of orientation at the vertex v, *i.e.* $b_0 = 0$ and $b_1 = 1$, the edges and facet keep the orientation they had on the initial polyhedron, *e.g.* yielding a looplet $(d_{13}, v, d_{12}|F_1^+)$ for facet F_1 in Fig. 4. In contrast, looplets are inverted in case of surface orientation change, *i.e.* when $b_0 = 1$ and $b_1 = 0$, *e.g.* yielding looplet $(d_{21}, v, d_{31}|F_1^-)$ for facet F_1.

4.3 Second Order Vertex Looplets

Second order vertices are the intersection of the edge of a polyhedron $\mathcal{P}_i$ and the facet of a polyhedron $\mathcal{P}_j$. As such it involves a total of three facets, one facet labeled F_2 from $\mathcal{P}_j$, and two

facets F_1 and F_3 from $\mathcal{P}_i$, adjacent to the edge yielding v from intersection with facet F_2. We here assume facet orientation as in Fig. 4, without loss of generality, because inverting normals of one of the two surfaces comes down to the same situation by swapping the roles of F_1 and F_3.

Four subvolumes defined by the crossing surfaces at the vertex define four boundaries between these subvolumes, each with two possible orientations. In the case of F_2, each of the two subvolume boundaries yields exactly one possible looplet in each orientation, e.g. for the top subvolume boundary in Fig. 4 the two possible looplets are $(d_{12}, v, d_{32}|F_2^+)$ and $(d_{23}, v, d_{21}|F_2^-)$. Any of the two mutually exclusive looplet orientations are generated for a given subvolume boundary, if the classification bits of the two subvolumes it separates have different values. In this case the looplet orientation is also given by these bits as the final surface normal points from the inside ($b_{**} = 1$) to the outside ($b_{**} = 0$) of the final volume.

The decision scheme is analogous for looplets of F_1 and F_3. Looplets of these facets are always simultaneously decided as they are determined by the same classification bits.

4.4 Third Order Vertex Looplets

The eight subvolumes surrounding v are separated by the three facets F_1, F_2, F_3. The configuration shown in Fig. 4 assumes that the normals of these three faces form a right-handed trihedron. This is again without loss of generality, should one of the facets have an opposite normal, a permutation in the order of the facets brings us back to this reference configuration. Because the looplet possibilities are analogous from one facet plane to another, we shall only enumerate the configurations for F_1. The enumeration also has a rotational symmetry within the facet plane, since it is divided in four quadrants by the other two facets. Fig. 4 shows that there are four possible looplets for a quadrant, bringing the total possible order-three looplet count to 48 for a vertex. We focus our description on one quadrant of F_1, classified as $(r, s) = (0, 0)$ by the two other facets (Fig. 4).

To ease the description, we introduce intermediate boolean predicates t_{rs}^+, t_{rs}^-, with $(r, s) \in \{0, 1\}^2$, two for each quadrant (r, s) of F_1. They indicate whether the quadrant represents a positive or negative boundary contribution in the plane of F_1. As such they are computed as $t_{rs}^+ := ((b_{0rs}, b_{1rs}) = (0, 1))$ and $t_{rs}^- := ((b_{0rs}, b_{1rs}) = (1, 0))$, testing opposing final volume classifications.

Note that quadrants cannot be individually decided here, because they are part of the same facet plane. The edges of the quadrant can thus delimit convex or concave planar corners, leading to different looplets. Consequently looplet decisions involve examining several quadrant boundary predicates. Concave looplets exist if three of the four quadrant boundaries exist for an orientation and the fourth doesn't, *i.e.* $(d_{13}, v, d_{12}|F_1^+)$ exists if $((t_{00}^+, t_{01}^+, t_{10}^+, t_{11}^+) = (0, 1, 1, 1))$, and $(d_{21}, v, d_{31}|F_1^-)$ exists if $((t_{00}^-, t_{01}^-, t_{10}^-, t_{11}^-) = (0, 1, 1, 1))$. On the other hand, convex looplets conditions depend only on three quadrant boundaries, the diagonally opposite quadrant in the facet having no influence; in fact diagonally opposite convex looplets of same orientation exist, as can be seen *e.g.* on v_2, v_3, v_4 and v_5 in Fig. 6. Concerning quadrant $(0, 0)$ in Fig. 4, convex looplet $(d_{21}, v, d_{31}|F_1^+)$ exists if $((t_{00}^+, t_{01}^+, t_{10}^+) = (1, 0, 0))$, while the opposing looplet $(d_{13}, v, d_{12}|F_1^-)$ exists if $((t_{00}^-, t_{01}^-, t_{10}^-) = (1, 0, 0))$.

4.5 Retrieving Final Polyhedron Facets

Once all vertices and their looplets have been generated, they can be re-indexed for each facet to generate its contributions to $\mathcal{P}_f$. We process each input facet separately, which improves the locality of the algorithm and reduces it to 2D. We illustrate this process in Fig. 7 and its result in Fig. 6, where the focus is on contributions of F_0. Within a finally contributing facet,

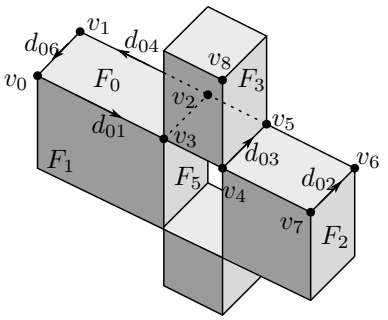

looplets
$(d_{06}, v_0, d_{01}\|F_0^+)$
$(d_{04}, v_1, d_{06}\|F_0^+)$
$(d_{05}, v_2, d_{04}\|F_0^+)$
$(d_{01}, v_3, d_{05}\|F_0^+)$
$(d_{30}, v_4, d_{01}\|F_0^+)$
$(d_{04}, v_5, d_{30}\|F_0^+)$
$(d_{02}, v_6, d_{04}\|F_0^+)$
$(d_{01}, v_7, d_{02}\|F_0^+)$
$(d_{05}, v_2, d_{40}\|F_0^-)$
$(d_{10}, v_3, d_{05}\|F_0^-)$
$(d_{03}, v_4, d_{10}\|F_0^-)$
$(d_{40}, v_5, d_{03}\|F_0^-)$

Figure 6: Result of the $(\mathcal{P}_1 \text{xor} \mathcal{P}_2) \cap \mathcal{P}_3$ operation on the example of Figure 3. The table lists the looplets for facet F_0.

an arbitrary seed looplet is chosen and its outgoing direction followed, iteratively searching for sequentially matching looplets to close the loop. In some occurrences, two or more looplets may match for a given direction: see for instance looplet $(d_{06}, v_0, d_{01}|F_0^+)$ in Fig. 6, for which both $(d_{01}, v_3, d_{05}|F_0^+)$ and $(d_{01}, v_7, d_{02}|F_0^+)$ match. In this case, the FIRST function selects the closest looplet in the search direction (here d_{01}). The whole process may be repeated until there are no looplets left in the face.

As noted previously, several convex, diagonally opposing looplets may be triggered for a same vertex, as is the case for *e.g.* v_3 or v_4 in $\mathcal{F}_1$. Both negative and positive orientation facets may be generated for a single input facet, and may even be adjacent and share an edge, as for F_0 in our example. Both of these configurations are typical of exclusive-or operations, but may happen with other operations. More generally, the algorithm can generate arbitrary output facets, with non-convex loops, several loops per facet (holes). Remarkably, our vertex-centered framework transparently accounts for all such possibilities.

4.6 2D topology of output facets

The processing cost for one facet of c corners (and hence c output vertices) is $\mathcal{O}(c \log(c))$, because the corners are sorted lexicographically by vertex index and offset on the edge. Even for simple input polygons, the number of generated vertices can be arbitrarily large, see for example Figure 20 or "dithering" in Figure 21.

At this stage the algorithm produced no superfluous geometry: all vertices and edges are required to represent the output polyhedron. However, non-convex polygons or polygons with non-0 genus are hard to manipulate, render or even feed back as input to the algorithm. Therefore, we typically tesselate the output facets to triangles or convex polygons. We use the very efficient GLU tesselator for this purpose.

5 Hierarchical Algorithm

The algorithm CSGVERTICES presented in the previous section is slow because it exhaustively considers all combinations of face triplets.

```
function CSGFacets
    Input: V_f: set of vertices of the output
    Output: L: final polyhedron facets as set of loops
    F := ∅, V := {}                          ▷ Set of contributing facets, and their vertices
    for v in V_f do                          ▷ Collect looplets for all vertices
        for F in AdjacentFacets(v) do
            F := F ∪ F+ ∪ F−                 ▷ Keep facets with both orientations
            V[F] := V[F] ∪ v                 ▷ Facet vertex contributions
        end for
    end for
    for F in F do                            ▷ Process each facet's two orientations
        l := ∅                               ▷ Looplets indexed by incoming direction
        for v in V[F] do                     ▷ Collect looplets for all vertices of F
            l := l ∪ ComputeLooplets(∗, v, ∗|F)
        end for
        while l ≠ ∅ do                       ▷ Looplets left for this facet
            (d_1, v, d|F) = pop(l)           ▷ Pick and remove a looplet
            F' := ∅                          ▷ Build this final facet
            repeat                           ▷ Chain looplet vertices
                F' := F' ∪ v
                (d', v, d|F) := First( (d, ∗, ∗|F) in l )
            until d = d_1                    ▷ Until back to start
            L := L ∪ F'                      ▷ Add this facet to final set
        end while
    end for
end function
```

Figure 7: Algorithm to find all facets of the result polyhedron from looplets.

A KD-tree is used to speed up the processing, and run CSGVertices only on leaves of the tree.

5.1 The KD-tree

The KD-tree is a binary tree where each node represents a bounding box and a set of polygons containing the input facets cropped by the bounding box. The bounding boxes of a parent node includes the bounding boxes of its child nodes. The exploration of the tree starts from the bounding box of all the polyhedra and stops splitting (leaf node) when there are few polygons (less than 20) left in the node. The function CSGVertices is called on the polygons of the leaves.

Like the vertices, nodes also have an indicator vector $\mathcal{M}$. Bit i of $\mathcal{M}$ has the following meaning:

- $\mathcal{M}_i = 0$: the full bounding box is outside $\mathcal{P}_i$
- $\mathcal{M}_i = 1$: the full bounding box is inside $\mathcal{P}_i$
- $\mathcal{M}_i = u$: this is an "unknown" bit, meaning that the bounding box is partially inside $\mathcal{P}_i$.

The node contains polygons from polyhedron $\mathcal{P}_i$ iff bit $\mathcal{M}_i = u$. We exploit this to split nodes and compute mesh positions efficiently using only information local to the node.

5.2 Splitting a node

Since the faces are convex, the polygons inside a node are also convex. The bounding box of a node is split in half along the axis with largest variance to produce the child nodes. The node's polygons are distributed to the two child nodes, and split in two if needed.

A child node inherits the mesh position from its parent, but if the parent contains polygons for $\mathcal{P}_i$ while the child has none, then $\mathcal{M}_i$ has to be changed from u to 0 or 1. In this case, necessarily $\mathcal{M}_i = u$ for the sibling child node because it inherited all the polygons from the parent.

In the example of Figure 8(a), the normal of the $\mathcal{P}_1$ polygons in child 1 are used to compute bit 1 of the mesh position of child 2. We need to find whether the splitting plane is inside or outside a mesh during the splitting pass. In this case it is applied to determine whether the face on the right of child 1 is inside of $\mathcal{P}_1$.

The orientation is given by the normal of one facet, the "extremal" facet. This facet is the one closest and most parallel to the splitting plane. For example, for the mesh in Figure 9, if v is the vertex with highest z coordinate, then the normal of gives the mesh orientation. This is tricky because the mesh is possibly open, it may be cut during the bounding box splits. Ray shooting cannot be used because it will be run in parallel, and different threads will not select the same ray.

We want to find the extremal facet in one pass over the facets of the mesh. During this pass, we keep track of the vertex v with highest z seen so far, $z_{\max}$. The polygons this vertex belongs to contribute two half-edges each. We intersect the half-edges with plane $z = z_{\max} - 1$, and project the extremal point v on the plane as v'. Each facet intersects with this plane as a segment and each half-edge as a point. Henceforth, we work in this 2D plane.

To find the extremal facet, we consider the edge most remote from v'. In Figure 9, this is e_{12}, its distance is $d_{\max}$. This leaves two possibilities for the extremal facet: F_1 or F_2. In the first example, both have the same normal orientation, so it does not matter, but in the second, their orientations are different.

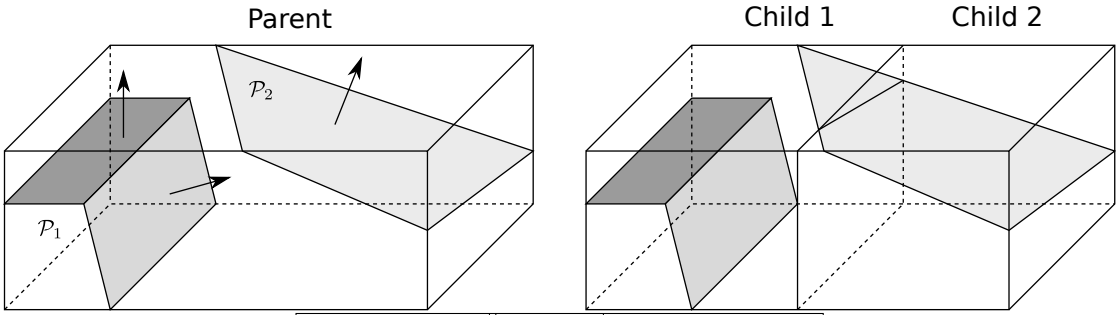

node	parent	child 1	child 2
mesh position	(u, u)	(u, u)	$(0, u)$

Figure 8: A KD-tree cell containing facets from $\mathcal{P}_1$ and $\mathcal{P}_2$ is split. The polygons stored in KD-tree cells are cropped to the cell.

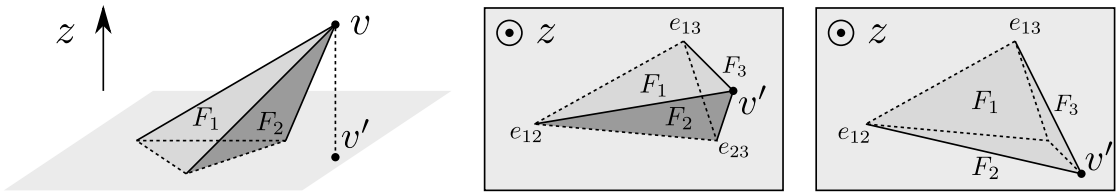

Figure 9: Finding a polyhedron's orientation in the positive z direction.

To choose between F_1 and F_2, we select the one whose slope is closest to orthogonal with (v', e_{12}). For example, the slope for F_1 is given by

$$s = \frac{| < (v' - e_{12})_\perp, e_{13} - e_{12} > |}{\|v' - e_{12}\|.\|e_{13} - e_{12}\|} \tag{11}$$

For the two half-edges contributed by each vertex in a facet, we compute (z, d, s). The triplets are compared lexicographically, ie. we compare d values only if the z values are the same. The maximum of the triplet gives the extremal facet. The current optimal triplet can be be maintained in one pass over the mesh facets, and triplets computed in different threads can be merged easily. Note that since the triplets for different facets are computed in the same way from the vertex coordinates, they are exactly the same: there are no roundoff errors to take care of when testing for equality.

5.3 Computing the indicator vector in a node

Once the mesh position $\mathcal{M}$ for a given node is known, computing the indicator vector $\mathbf{I}(x)$ for a point x inside this node can be done locally. The bit m_i of the vector is given by:

- if x is on a facet of polyhedron $\mathcal{P}_i$, then $m_i = s$
- if the node mesh position $\mathcal{M}_i \neq u$, the bit is $m_i = \mathcal{M}_i$

- otherwise ($\mathcal{M}_i = u$), we consider the non-empty set P of polygons of $\mathcal{P}_i$ in the node. We shoot a ray from x to an arbitrary point of one of the polygons to ensure at least one intersection with $\mathcal{P}_i$. Then we compute the intersection of this ray with all polygons of P an keep the intersection nearest to x. The sign of the dot product of the ray's direction with the normal at the closest point gives bit m_i.

The ComputeMeshPosition operation used in CSGVertices is uses this algorithm.

5.4 Pruning the KD-tree

At this point, we can explore the KD-tree and use the node-local vertex computations to compute the output vertices. An example is shown in Figure 10. The node mesh positions also make it possible to selectively explore the KD-tree.

For this, we extend f to handle undefined u values:

$$f : \{0, 1, u\}^n \to \{0, 1, u\} \tag{12}$$

It is often possible to compute $f(m)$ even if m contains u values. For example, for the intersection operation, if m contains a 0 at any position, then $f_\cup(m) = 0$; likewise for $f_\cap$. In general any expression based on the usual boolean operators can be expressed with a ternary boolean logic that includes an undefined state. A counter-example is f_{xor} where *all* the bits of M must be known to compute $f(m)$. This is a special case anyway because *all* double and triple points are selected by CSGVertices.

During the exploration of the KD-tree, there are two shortcuts that can be taken depending on the indicator vector $\mathcal{M}$ of the current node (see the red and blue nodes in Figure 10):

- if $f(\mathcal{M}) \neq u$, the node is completely inside or outside the output $\mathcal{P}_f$, so it does not contain any of its vertices and can be pruned.

- if $\mathcal{M}$ contains a single u bit (at position i) the output contains only primary vertices from $\mathcal{P}_i$. They can just be copied to the output. The input facets fully inside the bounding box are copied to the result, possibly with a reverted orientation. This is especially useful for large meshes with few facet-facet intersections.

As evidenced by the example of Figure 11, for large meshes, most of the geometry falls in these two cases.

6 Parallel implementation

In this section, we briefly describe the implementation, then we show how it was parallelized, with an efficient memory access model.

6.1 Implementation

We implemented the algorithm in C++. All coordinates are stored in 64-bit floats. The algorithms described in Sections 2 and 5 are augmented with various acceleration tricks (bounding box checking, avoiding duplicate vertex detections, early stops, lazy indicator computation, ...) The implementation is called **QuickCSG**. The main focus of the implementation is speed, which comes at a cost in terms of robustness (see Section 7.5).

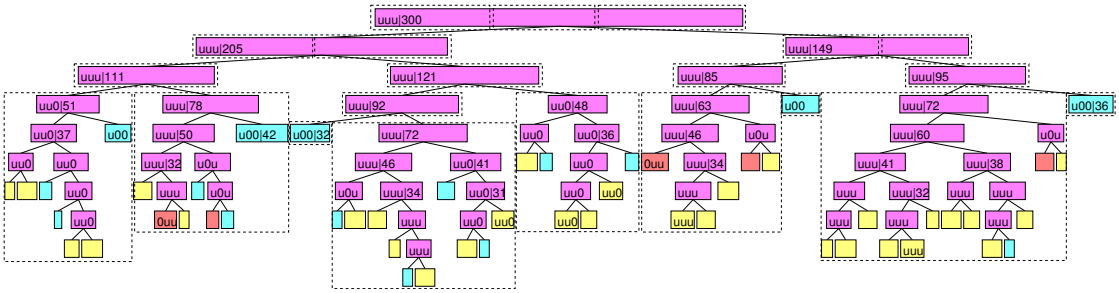

Figure 10: View of the KD-tree for operation $\mathcal{P}_f = \mathcal{P}_1 \backslash (\mathcal{P}_2 \cup \mathcal{P}_3)$ applied to three simple meshes. Each box represents a node, whose width is proportional to its number of polygons. When space allows, text in the box indicates node's indicator vector and the number of polygons. Color code: ■ = node that was split, ■ = leaf where vertices were found with CSGVERTICES, ■ = facets were just copied to the output, ■ = node was found completely inside or outside the mesh. Each dashed box represents a parallel task.

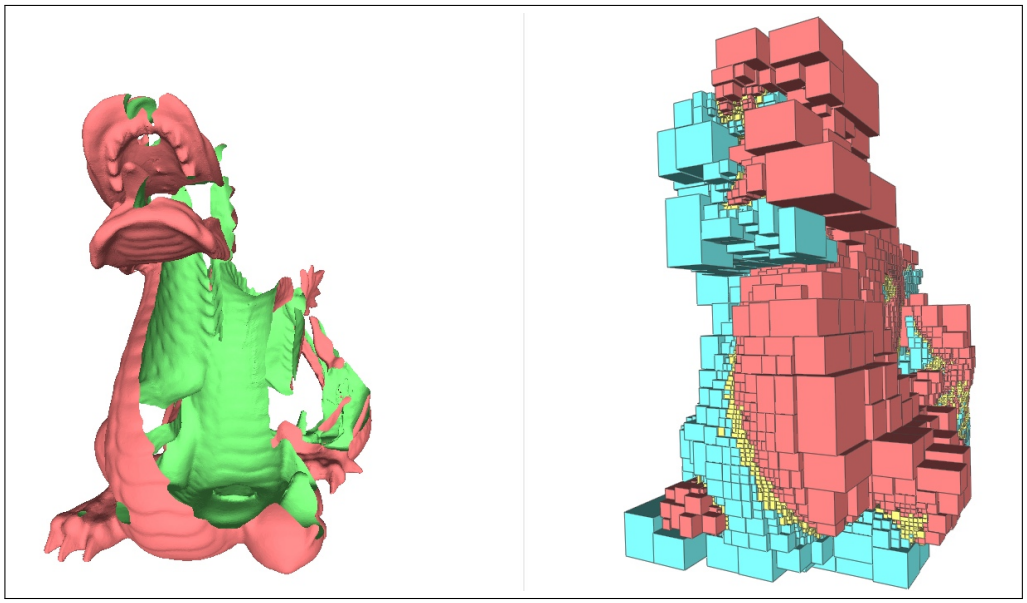

Figure 11: CSG difference between a red and a green dragon mesh, and bounding boxes of leaf nodes of the KD-tree. The color coding is the same as Figure 10.

6.2 Work stealing

Performance being a main concern, parallelisation is mandatory to take benefit of today's processors, all relying on multi-core architectures. The CSGFaces function is easily parallelizes with a parallel for. Function CSGVertices is more irregular: the workload associated with each node of the KD-tree is data-dependent and difficult to predict. The parallelisation must support dynamic load balancing of available cores, to ensure an efficient usage of the available resources.

For that purpose we rely on the task-based parallel programming paradigm and a work stealing task scheduling strategy. The programmer expresses the potentiel parallelism in his code by delimiting dynamically created tasks that can be executed concurrently. Each processing core maintains a list of tasks. When a core generates a task, it pushes it in its local list. A task of this list is ready for execution once synchronization constraints have been resolved. When a core becomes idle (no local task left), it randomly selects another core and steals part of the tasks ready to be executed in the task list of its target. If no task can be stolen, an other victim is targeted. This scheduling algorithm has proven performance [Blumofe and Leiserson, 1999]. Today, several parallel programming environments are based based on work stealing (Cilk, TBB, OpenMP, KAAPI) come with higher level constructions easing the parallelisation of common patterns (loop with independent iterations for instance). Their implementations ensures high performance on multi-core processors and shared memory machines. Our implementation relies on Intel's Thread Building Blocks (TBB).

6.3 Parallel tree exploration

The recursive nature of the KD-tree construction fits the task model well. The function that splits a node in two child nodes is encapsulated in a task. These tasks can be executed concurrently and work stealing ensures they are dynamically spread amongst enrolled cores.

The KD-tree construction starts with a single task. Enough tasks become available to keep all cores busy only once a certain depth is reached. Meanwhile, many cores will stall. To circumvent this bottleneck, the splitting of the toplevel nodes is paralellized internally, see Fig. 10. The loop testing the intersection of each vertex with the splitting plane is turned into a parallel loop and the results are accumulated in separate vectors for each thread. Since this is less efficient than the node-level parallelization, so it is used only in the very upper levels of the tree.

Creating a task comes with some overhead, that can become significant for nodes with a light compute load. This is the case for deep nodes where the number of tasks is much higher than the number of enrolled cores. Thus to shave off overheads, we turn to a sequential sub-tree exploration once the number of facets to process in a node is below a given threshold (80).

6.4 Memory considerations

When a node is split, the polygons are either split in two or transferred to one of the two children, ie. there is no duplicated data between parents and children. This limits the amount of RAM used for the polygons. However, all relevant information for CSGVertices is copied to the node structure. This avoids costly random accesses to the global facet and vertex tables.

The KD-Tree can be explored in any convenient order. In sequential sections, we choose a depth-first order, because it is cache friendly (a child is visited after its parent). The nodes are deallocated after they are visited so that only the path from root to current node resides in RAM at any moment.

This requires efficient dynamic memory allocation. For instance two new vectors are created when splitting a node to store each child node's faces. QuickCSG relies on (1) a vector implemen-

tation that does no dynamic allocation for small vectors (2) thread-local memory pools and (3) an allocator optimized for intensive concurrent memory allocations (`tbbmalloc`). This results in significant performance gains ($> 20\%$).

7 Experiments and discussion

In this section, we describe our test setup. Then we evaluate a few features of our algoritm: how it behaves in a parallel setting and how it performs compared to binary operations. We compare the algorithm to several state-of-the-art software packages, then discuss some failure cases. Finally, we show how it performs in two opposite application cases: in real time and when processing meshes with huge triangle counts.

Unless stated otherwise, we ran the experiments on a i5 CPU 750 at 2.7 GHz (4 cores) with 4 GB of RAM. The measured runtime is for the processing from input mesh to output mesh (excluding startup time and disk i/o) including tesselization to convex polygons. We measured the wall-clock times using the `gettimeofday` function, and found that timings for several single-thread runs are within 1% of each other, so we do not report standard deviations.

7.1 Test setup

For our experiments, we consider three operations on many meshes that intersect very often:

- T1: a set of 50 random toruses. We compute difference between the union of the 25 first toruses with the union of the 25 next ones: $\mathcal{P}_f = (A_1 \cup \cdots \cup A_{25}) \backslash (A_{26} \cup \cdots \cup A_{50})$. This is a typical CSG case, where there are many intersecting facets, but the geometry is regular (small compact facets).

- T2: a set of 50 concentric narrow random toruses. The toruses follow the great circles on a sphere, so each torus intersects each other torus in two locations. We compute the volumes where at least 2 of the toruses are present ($f_{\min-2}$). In this case, most facets intersect another. This generates many disconnected components with many more facets than there are on input.

- H: a set of 42 cones with arbitrary bases corresponding to the silhouettes of a piece of rope seen from 42 cameras. The silhouettes define cones whose apexes are the optical centre of the cameras, and that pass through the silhouette's shape on the camera's image planes. An approximation of the piece of rope can be reconstructed by intersecting ($f_\cap$) the cones [Franco and Boyer, 2009]. The facets are very elongated, and there are no primary vertices in the output mesh.

Table 12 gives some statistics about the datasets and the processing speed of QuickCSG. The "topology" stage does a pass over the data to register the neighborhood information of each facet, their normals, etc. The behavior can be different depending on the mesh. For T1 and H, the slowest stage is CSGVertices, for T2 it is CSGFacets, because it generates so many faces.

7.2 Properties of QuickCSG

Here we derive some properties of the algorithm that support the claims of the previous sections: it is efficient to perform CSG operations on multiple polyhedra in one pass, the complexity of the CSG operations is $\mathcal{O}(k' \log(N_\mathrm{f}))$, and the parallelization is efficient.

Input		
T1 $n = 50$, 40k vertices, 40k faces	T2 $n = 50$, 3500 vertices, 3500 faces	H $n = 42$, 16k vertices, 33k faces
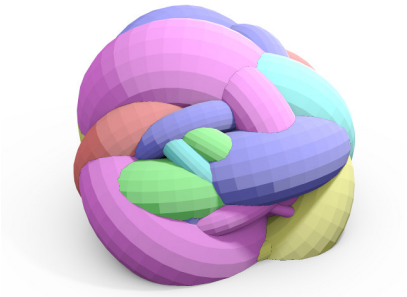	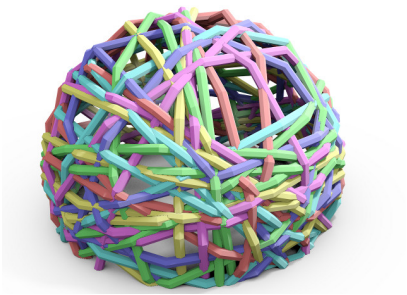	
Ouput		
2 components, 16k vertices, 32k faces	123 components, 47k vertices, 94k faces	13 components, 27k vertices, 14k faces
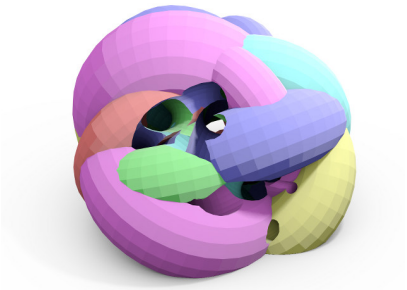	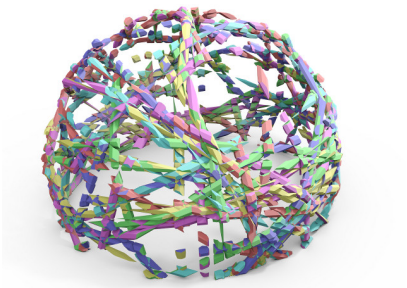	
QuickCSG runtime (topology + CSGVERTICES + CSGFACETS = total) and memory usage		
7.1 + 69.9 + 10.4 = 87.4 ms 61 MB RAM	0.9 + 78.3 + 72.5 = 151.7 ms 45 MB RAM	5.1 + 437.6 + 26.2 = 468.9 ms 96 MB RAM

Figure 12: Statistics on the tested datasets, and views of the 3 output meshes. RAM is measured as the maximum resident set size reported by the unix `time` utility.

T1		
ordering	time	errors
single	0.125	0
binary tree	0.363	0
sequential	0.619	0
5,5,2	0.180	0
25,2	0.111	0

H		
ordering	time	errors
single	0.524	0
binary tree	2.396	9147
sequential	2.244	50258
8,6	0.674	0
4,11	0.872	0

Figure 13: Execution time of several ways of expressing the same CSG operation on the datasets T1 and H in multithreaded mode.

7.2.1 Comparison with binary CSG operations

Any associative boolean operation f can be expressed as a sequence of $n-1$ binary operations, either sequentially or in a binary tree:

$$\begin{aligned} f(a_1, \cdots, a_n) &= f(a_1, f(a_2, \cdots f(a_{n-1}, a_n) \cdots)) \\ &= f(\cdots f(a_1, a_2) \cdots, \cdots f(a_{n-1}, a_n) \cdots)) \end{aligned} \tag{13}$$

These decompositions produce $n-2$ intermediate polyhedra.

The CSG operations on T1 and H can be expressed with binary operations. We compared the speed of several organizations of the computation, see Table 13 (numbers are slightly different from Figure **??** because they are done via the Python interface of QuickCSG). Using binary operations is clearly slower than a single operation, because it produces many facets of intermediate polyhedra that are discarded later on. The binary operations also increase the probability of errors caused by degeneracies (see Section 7.5). On the other hand, operating on fewer meshes means that fewer vertex/cell position bits need to be computed.

We investigated the trade-off between a single operation and a binary tree of operations. We do this by starting from the binary tree version and increasing the arity of the tree. In Table 13, for example "25,2" in T1 means that we compute the union of the 25 first polyhedra, then the 25 last ones, then the difference between the two intermediate polyhedra, and likewise for other experiments. The results show that it is generally faster to perform the CSG operation in one pass, except for T1, where the "25,2" ordering gives better results.

7.2.2 Parallelization

Figure 14 shows how the parallel processing proceeds. In the beginning, the splitting of the top-level nodes is hard to parallelize, until there are enough tasks to run on all cores. The CSGFacets stage parallelizes easily. The sequential interval between them is the distribution of vertices to each face to consider. It is so memory-intensive that it is not attractive to parallelize it. The behavior is dependent on the geometry of the scene, eg. for T2, the number of output facets is much higher than the input facets, which explains the relatively high importance of the CSGFacets stage.

Figure 15 shows that, depending on the geometry of the scene, the speedup is more or less linear with the number of threads. At best, a speedup of 20× can be obtained with 48 cores. Note that the performance reported in Figure 14 is not as good due to the code instrumentation to gather statistics.

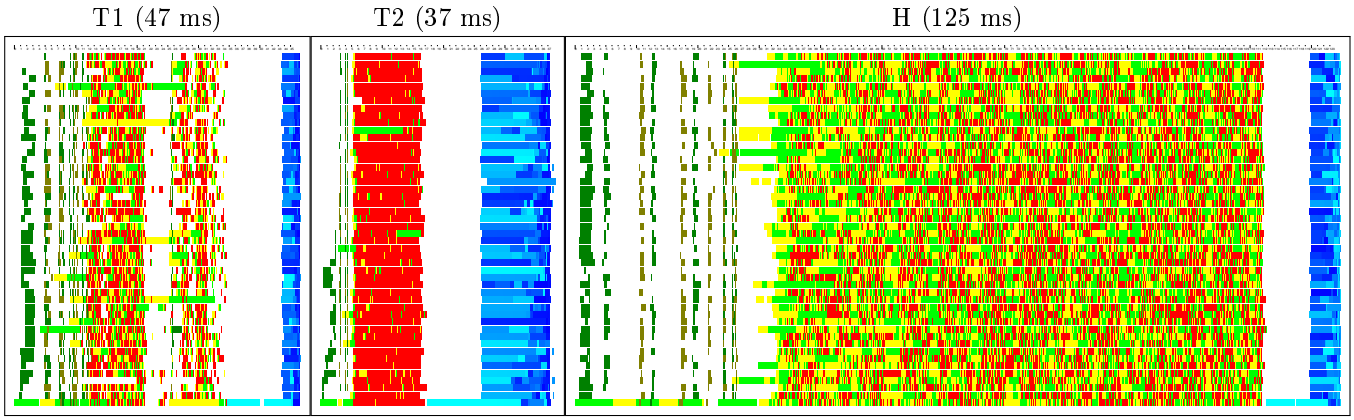

Figure 14: Occupation of a 48-core AMD processor during the computation: x-axis = time, y-axis = cores. Each colored rectangle represents a task. Green/yellow = node splitting, red = CSGVERTICES applied to a tree leaf, shades of blue = building facets (CSGFACETS).

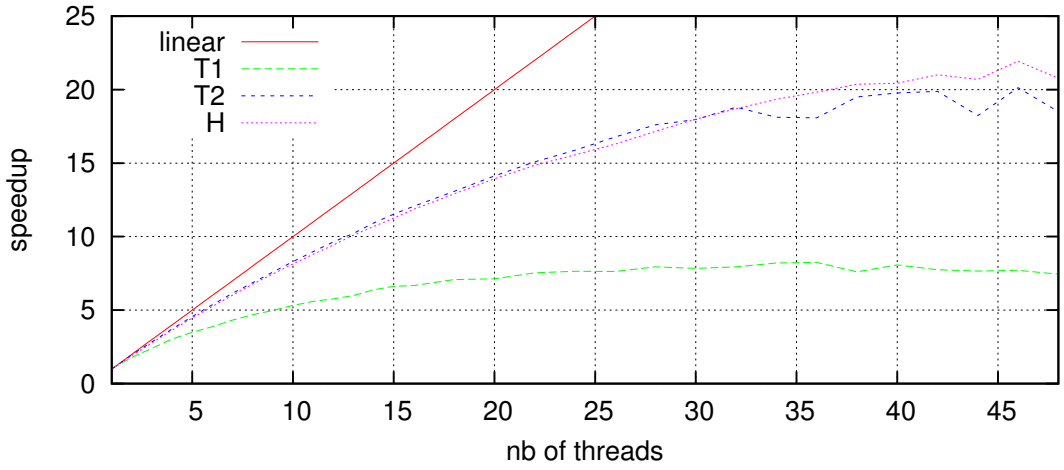

Figure 15: Speedup obtained with more threads, with respect to a sequential run. This is measured on a 48-core AMD Opteron(tm) Processor 6174.

7.3 Comparison with the state of the art

We compare QuickCSG with other CSG implementations described in recent papers and software packages. To ensure a fair comparison, we aim at reproducing the experimental setups from the papers, normalizing the hardware differences (in particular, using the same number of threads), and comparing the reported timings with ours. We obtained the input data either by communicating with the authors, or from the Stanford 3D scanning repository, resizing the meshes to the detail level reported in the papers if necessary.

Most other papers compared with publicly available CSG implementations like CGAL or GTS [Feito et al., 2013], or with CSG implementations from commercial packages like Rhino, ACIS [Wang, 2011], Houdini [Pavic et al., 2010] and 3DS Max [Feito et al., 2013]. Since these packages were found to be many times slower than the research implementations, we concentrate on the comparison with the latter.

We did also a few applicative experiments, where QuickCSG is integrated for 3D reconstruction, 3D printing and collision detection.

7.3.1 Carve CSG

Carve is the CSG library[1] used in the Blender modeler. It uses a KD-tree accelerator structure and produces clean output meshes, with few useless vertices. We compare the algorithms on the slowest operations in the Carve CSG test suite (`test_intersect.cpp`), that handle large meshes or/and many meshes. Since Carve CSG is not multithreaded, we compared it against QuickCSG with a single thread. The timings are:

Example	N_f	Carve	QuickCSG
21: sphere − translated sphere	19600	0.342	0.077
29: union of 30 rotated cubes	180	0.495	0.077
30: sphere − sphere ∩ cube	19606	0.469	0.032
34: cow ∪ translated cow	185728	3.601	0.313

Hence, QuickCSG is 4 to 14 times faster than Carve on examples of its test suite.

7.3.2 A GPU implementation

We compared with an approximate GPU implementation of CSG operations [Wang, 2011], that uses an octtree as accelerator structure. We tested the author's implementation (MeshWorks[2]) on examples provided along with the software, mostly from the Stanford 3D scanning repository. This was about 15 slower than QuickCSG in our tests (Dragon ∪ Bunny):

Example	N_f	[Wang, 2011]	QuickCSG
Dragon ∪ Bunny	941k	55.4	3.4
Small dragon − Bunny	347k	3.06 – 8.97	0.253
Buddha ∪ Vase-Lion	1.48M	10.68 – 21.81	1.027

Therefore, we also compared with the results reported in their paper (second and third example). Taking into account a 1.25 speed factor between the CPUs, QuickCSG with 4 threads is between 8 and 20 times faster than Meshworks, depending on Meshwork's quality setting. Note that the input meshes have small self-intersections, so QuickCSG's output contains holes, see Figure 19.

[1] Carve 1.4 can be found at `http://code.google.com/p/carve/downloads/list`.
[2] Executable at `http://www2.mae.cuhk.edu.hk/~cwang/projMeshWorks.html`

MeshWorks is optimized for large and detailed meshes. In this case, most faces do not intersect another face, so it is important to copy these from input to output quickly. MeshWorks and QuickCSG both do this, but is seems that the up- and down-load to the GPU hurts the performance.

7.3.3 Hybrid Booleans

The "Hybrid booleans" method of [Pavic et al., 2010] subdivides the input space in octrees in a very similar way to our method. Then it constructs an approximate output mesh using their Extended Dual Contouring method. We applied our QuickCSG implementation on their test data, and compare it against the timings they report. The test machines are almost the same, we disabled threading for QuickCSG and measure computation time in seconds:

Example	N_f	[Pavic et al., 2010]	QuickCSG
Chair	1.5k	1.3 – 13	0.003
Sprocket	11k	5 – 47	0.069
Organic	219k	1.6 – 24 (+1)	0.488

Depending on the quality settings of [Pavic et al., 2010], QuickCSG (which gives an exact result) is 5 to more than 100 times faster. The hybrid booleans method is hampered by the fact that it requires to explore the tree to a predefined depth even for the simplest of input meshes (the "Chair" example). It also generates a large amount of over-tesselated polygons. The "Organic" example is based on the CSG operation $(\mathcal{P}_1 \backslash \mathcal{P}_2) \cup (\mathcal{P}_3 \backslash \mathcal{P}_4) \cup (\mathcal{P}_5 \backslash \mathcal{P}_6)$. QuickCSG computes it in a single pass over the data, while it is computed on with intermediate meshes in [Pavic et al., 2010] (the +1s accounts for the intermediate computation).

7.3.4 Feito et al

We compare with [Feito et al., 2013]. Their algorithm implements of two-component boolean expressions on triangular meshes, and is based on a parallel exploration of an octtree. They evaluate their algorithm by combining standard meshes (the dragon, the armadillo) with a translated version of the same mesh. They test four CSG operations (union, intersection, and difference in the two senses) and average timings over the four. They ran their tests on a computer with the same clock frequency as our test machine (but with more cores and RAM). The comparison gives (th = # threads):

Example	N_f	[Feito et al., 2013]			QuickCSG	
		1 th	4 th	16 th	1 th	4 th
Armadillo	2×150k	2.71	1.46	0.68	0.57	0.24
Dragon	2×871k	12.64	6.48	2.72	2.61	1.18

QuickCSG is 4 to 5 times faster with the same number of cores, QuickCSG with 1 thread is similar to [Feito et al., 2013] with 16 threads. Since the algorithms are quite similar, the two possible explanations are that their algorithm generates too much intermediate geometry (over-tesselized triangles and vertices that must be merged in a later stage), and that their KD-tree is completely stored in RAM, since it is used for the ray shooting. Our KD-tree is deallocated as soon as explored, see Section 6.4.

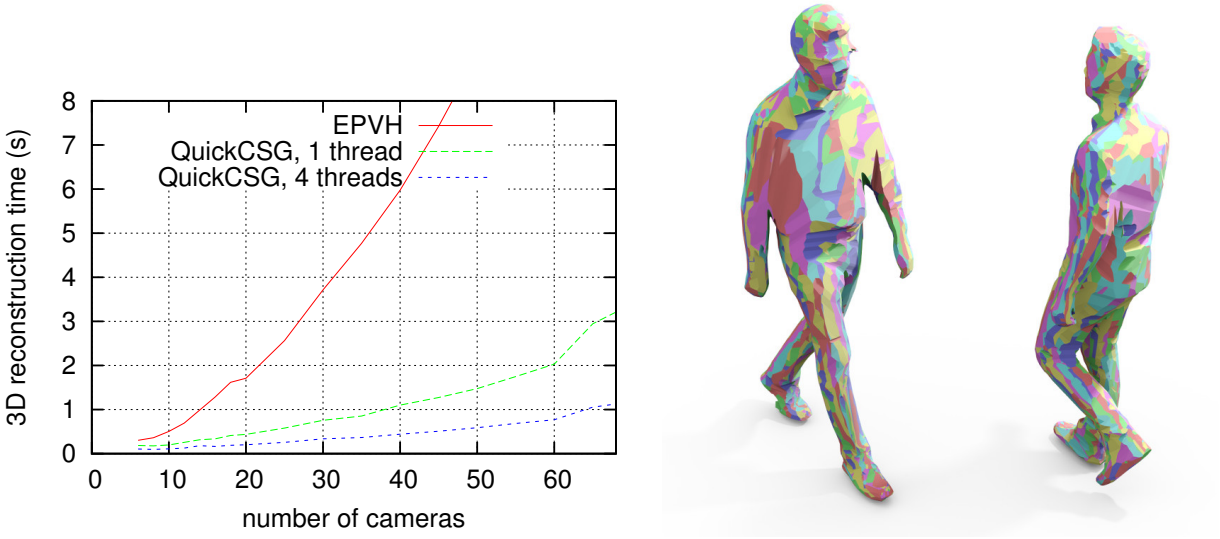

Figure 16: Left: runtime for a 3D reconstruction from visual hulls, a CSG intersection between viewing cones. The scene remains the same but we vary the number of cameras, and hence the number of input polyhedra. Right: the reconstruction result with 68 cameras (22k facets).

7.3.5 EPVH

EPVH [Franco and Boyer, 2009] is a silhouette-based 3D reconstruction method. It intersects a set of viewing cones corresponding to the silhouette viewpoints. We compare the original implementation on the a set of 68 silhouettes captured in a 3D capture studio[3], varying the number of cameras used to do the reconstruction: more cameras provide a better reconstruction. This is similar to the H example, but to speed up QuickCSG for this case, we start with open polyhedra: the base of the cone is not included. Since the cones are infinite, we crop them to the bounding box of the scene (which is assumed to be known), and set the root of the KD-tree to this bounding box.

Figure 16 shows that QuickCSG with 1 thread is 4 to 6 times faster than the highly specialized method of [Franco and Boyer, 2009]. Note that there is a discontinuity at 64 cameras, because QuickCSG switches from one to two 64-bit words to store the indicator vectors.

7.3.6 OpenSCAD

OpenSCAD[4] is a solid modeling software where all solids are represented as boolean combinations of primitive shapes (cylinder, sphere, extruded 2D shapes, etc.). It is typically used to design arbitrary objects for 3D printers.

In the OpenSCAD language, the boolean operations are nodes of a binary tree, whose leaves are the primitives. The shape can be "rendered" to a polygonal mesh. We implemented a parser for a subset of the OpenSCAD language that calls QuickCSG with a function f that computes a

[3] `http://kinovis.inrialpes.fr`
[4] `http://www.openscad.org/documentation.html`

tree of boolean operations. We run our renderer on two complex models, "balljoint" and "doggie", that were exported from IceSL [Lefebvre, 2013]. We printed the mesh generated from balljoint using Makerware on a Makerbot Replicator 2 (Figure 17). All the balljoints are functional.

OpenSCAD's default renderer, based on CGAL [Hachenberger et al., 2007] is slow: 16 minutes and 7 minutes for balljoint and doggie, respectively vs. QuickCSG's 3.8 s and 0.32 s. The speed advantage of QuickCSG comes at a cost: workarounds are required to avoid degeneracies (see Section 7.5), which still let through a few errors.

In contrast with the examples of Section 7.2.1, it is not optimal to compute the whole result at once, as this does not exploit the inherent geometrical locality of the CSG tree. To evaluate the trade-off between binary and all-at-once computation, we traverse the OpenSCAD CSG tree, returning an intermediate sub-tree for each node. For a given node, we collect the result sub-trees of its two child nodes. If the total number of meshes in these sub-trees is above some threshold G (the grouping factor), we call QuickCSG to compute the CSG operation and return a 1-node sub-tree with the CSG result. Otherwise, we return a sub-tree built with the two child mesh results and the binary operation. The binary evaluation baseline is obtained with $G = 2$, it just replaces the CGAL binary CSG operator with the QuickCSG one.

The plot in Figure 17 shows the execution time as a function of the grouping factor G. The optimum, for $G = 8$, runs balljoint in 0.96 s and doggie in 0.20 s, which is 30% faster than the binary evaluation. This is a good result, given that the OpenSCAD model is built with binary CSGs in mind, ie. there is little interaction between distant subtrees of the CSG tree.

7.3.7 Collision detection

Given a set of solids, collision detection can be performed by computing the min-2 operation. Each connected component of the output is an area where at least two solids collide. The forces resulting from the collision can be computed from the volume and center of mass of these connected components. This approach is limited, because it does not handle self-intersections and gives ambiguous results on volumes where three or more solids intersect.

As a small experiment, we ran QuickCSG on an example of the SOFA physical simulation engine[5]. During the simulation, two flabby octopuses pass through four rings, see Figure 18. The detection takes 15.5 ms (excluding the 6 ms topology pass, which can be run once at the beginning of the animation). The state-of-the-art method of [Allard et al., 2010] computes collisions and friction in 5 ms on the same example, but it is GPU-based and relies on a layered depth image that produces approximate intersections.

7.4 Comparison on our test examples

The previous experiments were run on examples provided with state-of-the-art packages. This can be assumed to be their "confort zone". For this experiment we select Carve CSG, which is one of the fastest packages, to run on *our* test cases. We test on T1, T2, H and a larger example, "dithering", see Figure 21.

For testing with Carve, we expressed T1, H and dithering as trees of binary operations. For completeness, we also tried to express T2 as the union of all intersections of 2 meshes, amounting

[5] `http://www.sofa-framework.org`.

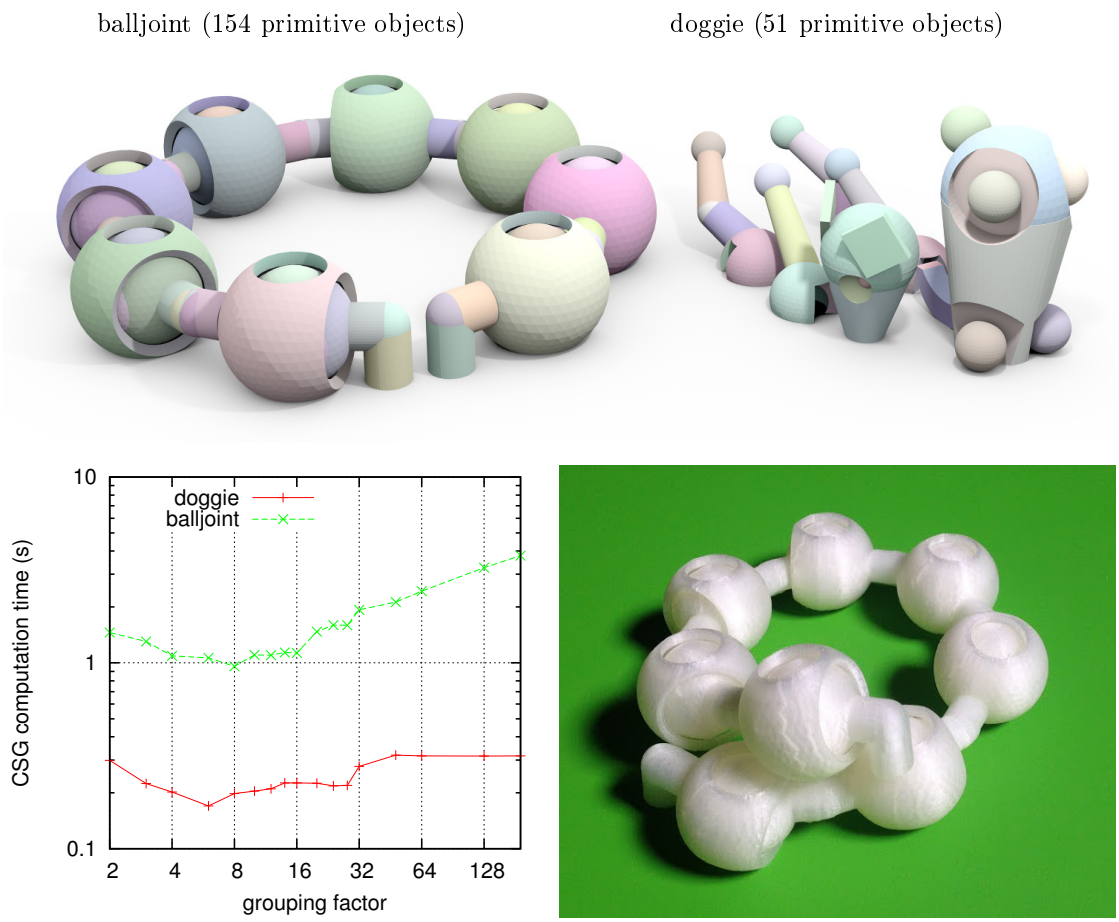

Figure 17: Above: OpenSCAD models balljoint and doggie. Below: CSG computation time (single thread) depending on the grouping strategy, and printed version of the balljoint.

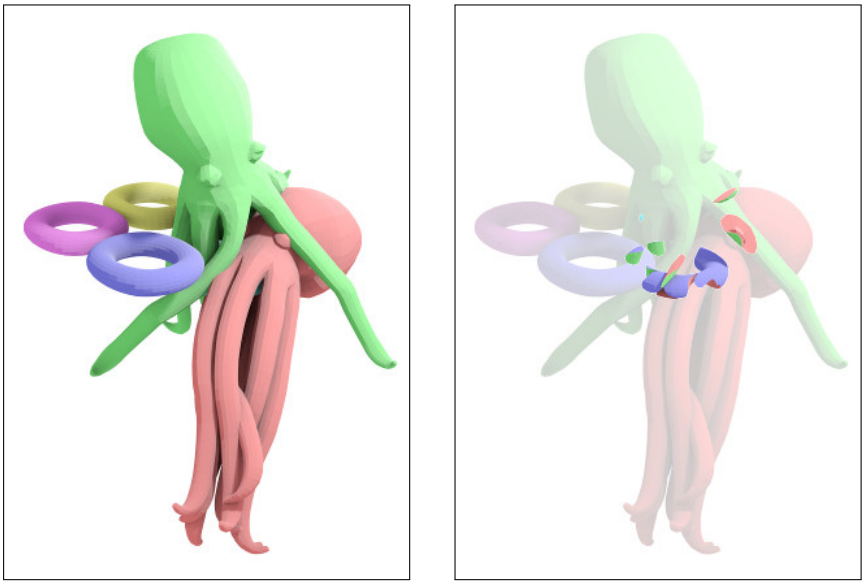

Figure 18: Collision detection using QuickCSG with the min-2 operation on six solids (33k faces in total).

to $\binom{n}{2}$ components:

$$\begin{aligned} f_{\min-2}(a_1, \cdots, a_n) = \\ f_\cup(f_\cap(a_1,a_2), & f_\cap(a_1,a_3), \cdots, f_\cap(a_1,a_n), \\ & f_\cap(a_2,a_3), \cdots, f_\cap(a_2,a_n), \\ & \cdots \qquad\quad f_\cap(a_{n-1},a_n)) \end{aligned} \tag{14}$$

Computing the unions of the intermediate intersections generates many degeneracies because they come from the same input meshes. Despite its careful handling of degenerate cases, Carve was not able to compute $f_{\min-2}$ on more than 38 input meshes. The results, again without threads, are:

Example	N_f	Carve CSG	QuickCSG
T1	40000	4.652	0.297
T2	3500	(94.795)	0.596
H	33108	26.330	1.720
dithering	1743634	(643.891)	5.647

Thus, for T1 and H, QuickCSG is 15 times faster. The timing indicated for "dithering" is only for the intermediate operation that computes the mask, as it is unable to handle the full computation. For T2 and "dithering", QuickCSG is at least 100 times faster.

7.5 Failure cases and workarounds

QuickCSG relies on the hypotheses on the input meshes: non-degeneracy and watertightness. Simple meshes modeled by humans tend to have degenerate configurations (tangent faces, aligned

edges, etc.). Also, many large meshes have local errors: missing triangles, small self-intersections, etc.

Similar to [Wang, 2011, Feito et al., 2013], we observed that many CSG implementations (like CGAL and Carve CSG) crash or refuse to process meshes that they cannot handle completely. The approach in QuickCSG is to record the errors that are encountered during processing and report them, while still producing a possibly incomplete output mesh. These result in the error counts reported in the previous experiments.

7.5.1 Types of errors

We encountered three main sources of errors:

- invalid inputs (self-intersecting or non-watertight meshes) can have catastrophic consequences if a self-intersecting facet is used to determine the mesh position of a KD-tree node (see Section 5.2) and causes a useful node to disappear, see Figure 19. "Catastrophic" means that the extent of the error can be arbitrarily large.
- degeneracies cause some output vertices not to be found, which in turn produces "incomplete loops", ie. the algorithm cannot produce the corresponding facet. Therefore, the output mesh is not watertight. The holes expand if the output mesh is re-used as input for another CSG computation.
- since the KD-tree is axis-aligned, axis-aligned facets may also produce degeneracies. A simple workaround is to apply a random rotation to the input and revert this rotation at the end.

7.5.2 Workarounds

In some of the previous experiments, we used a simple workaround to avoid degeneracies: we translate each input mesh by a random vector of length ε_1. Then we run QuickCSG. At the end of the computation, we reset the first order vertices to their initial positions. Second and third order vertices can be expressed as an edge-facet intersection or the intersection between 3 facets. Therefore, the exact vertex positions are recovered by recomputing the intersections. For this to work, the magnitude ε_1 must verify $\varepsilon_2 \ll \varepsilon_1 < \varepsilon_3$, where ε_2 is the precision where intersection computations start to become inaccurate, and ε_3 is the smallest distance between two vertices in the input meshes.

7.6 Real-time CSG and huge meshes

To showcase our algorithm we applied it to two opposite cases: for real-time CSG computation and to compute CSG operations on larger meshes.

For the first experiment, we developed a small Python OpenGL application that animates three sets of quasi-parallel boxes and computes a CSG on them in real time, see Figure 20. The animation runs smoothly for 3×10 boxes. This CSG operation generates many more output triangles than there were on input. In the case of min-2, the output is a $10 \times 10 \times 10$ grid of 3D crosses, see Figure 20.

A few larger-scale examples are shown in Figure 21. The "dithering" example mixes two dragon meshes $\mathcal{P}_1$ and $\mathcal{P}_2$ with a 3D dithering pattern. The pattern is defined as the union of three orthogonal combs: $D = \mathcal{P}_3 \cup \mathcal{P}_4 \cup \mathcal{P}_5$. Then the dragon meshes are combined using the pattern as a mask: $\mathcal{P}_f = (\mathcal{P}_1 \cap D) \cup (\mathcal{P}_2 \backslash D)$. The "serpent" example is a fractal where a tube, $\mathcal{P}_1$, is wound around a torus (not shown). Then another tube, $\mathcal{P}_2$, winds around $\mathcal{P}_1$ and so on

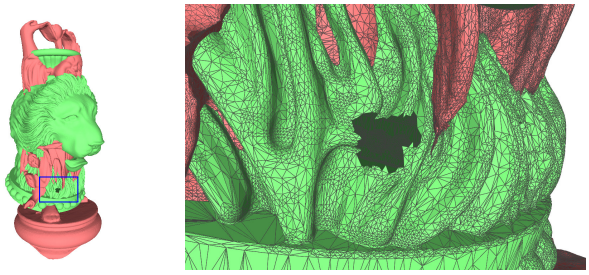

Figure 19: Failure case: when computing the union between two meshes, the algorithm makes a mistake on the mesh position of a KD-tree node because the input mesh is invalid (self-intersecting). Left: the result, right: close-up of the hole in the mesh (the example is "Buddha ∪ Vase-Lion" from Section 7.3.2).

until $\mathcal{P}_5$. We compute the min-2 operation. The results has a topological genus [Agoston, 2005] of 701, i.e., it can be transformed without tearing into a sphere with this many handles.

The last example is built from six instances of the "Happy Buddha" mesh [Curless and Levoy, 1996], the largest mesh from the Stanford repository. We intersect these with the union of 100,000 random spheres. The spheres were labeled with a greedy graph coloring algorithm to group them into 37 disjoint subsets, so there are a total of 43 input meshes and 24 M triangles. The CSG operation computes the union of the 6 Buddhas and intersects this with the union of all spheres: $\mathcal{P}_f = (\mathcal{P}_1 \cup \cdots \cup \mathcal{P}_6) \cap (\mathcal{P}_7 \cup \cdots \cup \mathcal{P}_{43})$. It is run on a 12-core Mac Pro machine with 64 GB of RAM (it uses to much memory for our standard test machine) in 8 s. The result of 5 M triangles, is shown on Figure 1.

8 Conclusion

Our CSG algorithm for polyhedra represented as vertices and facets is simple and more general than the state of the art. The QuickCSG implementation is several times faster than any other implementation we are aware of. It can be parallelized easily and efficiently.

On the web page `http://pascal.inrialpes.fr/data2/douze/QuickCSG/` we provide the input meshes and command lines for most experiments, an executable version of QuickCSG and a few more result images.

As future work, we plan to distribute the CSG computation over several machines. Ultimately, we want to use QuickCSG to do real-time 3D reconstruction with many complex input meshes.

Acknowledgements

We are grateful to Edmond Boyer, François Faure and Stan Borkowski for fruitful discussions. We thank Marcel Campen, Charlie Wang, Sylvain Lefebvre and Matthieu Nesme for providing us their test data. We used the extraordinarily versatile MeshLab software to visualize, convert and repair polyhedra, and the excellent Blender modeler for rendering. We thank the Equipex projects Kinovis and Amiqual4Home (ANR-11-EQPX-0002) for letting us use hardware.

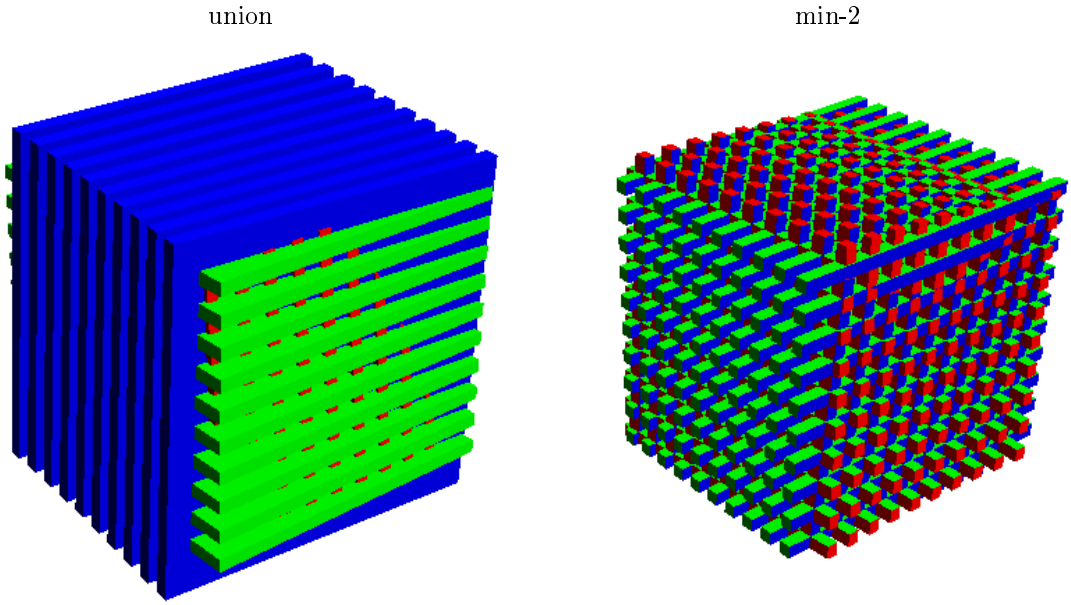

Figure 20: Animated CSG of 3×10 undulating boxes that generates 27k triangles. The animation runs at 30 fps.

References

[Adams and Dutré, 2003] Adams, B. and Dutré, P. (2003). Interactive boolean operations on surfel-bounded solids. *ACM Trans. Graph.*, 22(3):651–656.

[Agoston, 2005] Agoston, M. K. (2005). *Computer Graphics and Geometric Modeling*. Springer, London.

[Allard et al., 2010] Allard, J., Faure, F., Courtecuisse, H., Falipou, F., Duriez, C., and Kry, P. (2010). Volume Contact Constraints at Arbitrary Resolution. *ACM Transactions on Graphics*, 29(3).

[Baumgart, 1974] Baumgart, B. G. (1974). *Geometric Modeling for Computer Vision*. PhD thesis, Stanford, CA, USA. AAI7506806.

[Bernstein and Fussell, 2009] Bernstein, G. and Fussell, D. (2009). Fast, exact, linear booleans. *Computer Graphics Forum*, 28(5):1269–1278.

[Blumofe and Leiserson, 1999] Blumofe, R. D. and Leiserson, C. E. (1999). Scheduling multithreaded computations by work stealing. *J. ACM*, 46(5):720–748.

[Braid, 1975] Braid, I. C. (1975). The synthesis of solids bounded by many faces. *Commun. ACM*, 18(4):209–216.

[Brunet and Navazo, 1990] Brunet, P. and Navazo, I. (1990). Solid representation and operation using extended octrees. *ACM Trans. Graph.*, 9(2):170–197.

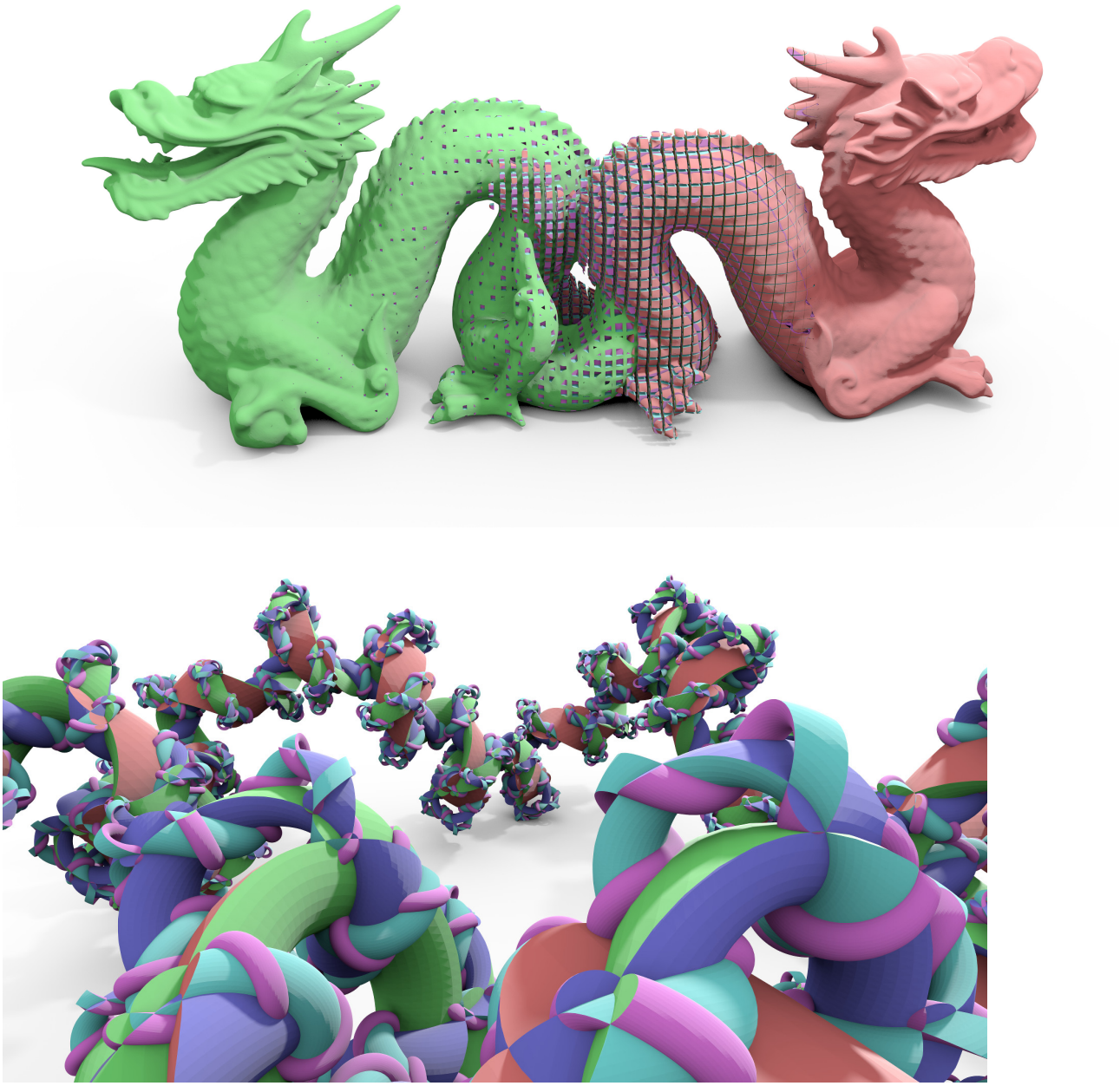

Figure 21: Extra example results of our algorithm: dithering (1.5M triangles) and serpent (10M triangles).

[Campen and Kobbelt, 2010] Campen, M. and Kobbelt, L. (2010). Exact and robust (self) intersections for polygonal meshes. *Comput. Graph. Forum*, 29(2):397–406.

[Carlbom, 1987] Carlbom, I. (1987). An algorithm for geometric set operations using cellular subdivision techniques. *IEEE Computer Graphics and Applications*, 7(5):44–55.

[Curless and Levoy, 1996] Curless, B. and Levoy, M. (1996). A volumetric method for building complex models from range images. In *SIGGRAPH*.

[Edelsbrunner and Mücke, 1990] Edelsbrunner, H. and Mücke, E. P. (1990). Simulation of simplicity: A technique to cope with degenerate cases in geometric algorithms. *ACM TRANS. GRAPH*, 9(1):66–104.

[Feito et al., 2013] Feito, F., Ogayar, C., Segura, R., and Rivero, M. (2013). Fast and accurate evaluation of regularized boolean operations on triangulated solids. *Computer-Aided Design*, 45(3):705 – 716.

[Franco and Boyer, 2009] Franco, J. and Boyer, E. (2009). Efficient polyhedral modeling from silhouettes. *Pattern Analysis and Machine Intelligence, IEEE Transactions on*, 31(3):414–427.

[Franco et al., 2013] Franco, J.-S., Petit, B., and Boyer, E. (2013). 3D Shape Cropping. In *Vision, Modeling and Visualization*, pages 65–72, Lugano, Switzerland. Eurographics Association.

[Hachenberger et al., 2007] Hachenberger, P., Kettner, L., and Mehlhorn, K. (2007). Boolean operations on 3d selective nef complexes: Data structure, algorithms, optimized implementation and experiments. *Comput. Geom. Theory Appl.*, 38(1-2):64–99.

[Hoffmann, 2001] Hoffmann, C. (2001). Robustness in Geometric Computations. *JCISE*, 1:143–155.

[Hoffmann, 1989] Hoffmann, C. M. (1989). *Geometric and Solid Modeling: An Introduction*. Morgan Kaufmann Publishers Inc., San Francisco, CA, USA.

[Laidlaw et al., 1986] Laidlaw, D. H., Trumbore, W. B., and Hughes, J. F. (1986). Constructive solid geometry for polyhedral objects. In *Computer Graphics (Proceedings of SIGGRAPH 86)*, volume 20, pages 161–170.

[Lefebvre, 2013] Lefebvre, S. (2013). IceSL : A GPU Accelerated modeler and slicer. In *18th European Forum on Additive Manufacturing*. `http://webloria.loria.fr/~slefebvr/icesl`.

[Li et al., 2004] Li, C., Pion, S., and Yap, C. (2004). Recent progress in exact geometric computation. *J. of Logic and Algebraic Programming*, 64(1):85–111. Special issue on "Practical Development of Exact Real Number Computation".

[Mäntylä, 1987] Mäntylä, M. (1987). *An Introduction to Solid Modeling*. Computer Science Press, Inc., New York, NY, USA.

[Naylor et al., 1990] Naylor, B., Amanatides, J., and Thibault, W. (1990). Merging bsp trees yields polyhedral set operations. In *Proceedings of the 17th Annual Conference on Computer Graphics and Interactive Techniques*, SIGGRAPH '90, pages 115–124, New York, NY, USA. ACM.

[Nef, 1978] Nef, W. (1978). *Beiträge zur Theorie der Polyeder: mit Anwendungen in der Computergraphik*. Beiträge zur Mathematik, Informatik und Nachrichtentechnik. Lang.

[Pavic et al., 2010] Pavic, D., Campen, M., and Kobbelt, L. (2010). Hybrid booleans. *Computer Graphics Forum*, 29.

[Popinet, 2006] Popinet, S. (2006). GNU triangulated surface library.

[Requicha, 1977] Requicha, A. A. G. (1977). Mathematical Models of Rigid Solid Objects. Technical Report TR-28, Production Automation Project, University of Rochester.

[Requicha and Voelcker, 1985] Requicha, A. A. G. and Voelcker, H. (1985). Boolean operations in solid modeling: Boundary evaluation and merging algorithms. *Proceedings of the IEEE*, 73(1):30–44.

[Requicha, 1980] Requicha, A. G. (1980). Representations for rigid solids: Theory, methods, and systems. *ACM Comput. Surv.*, 12(4):437–464.

[Sargeant, 2011] Sargeant, T. (2011). Carve csg boolean library, version 1.4.

[Schneider and Eberly, 2003] Schneider, P. and Eberly, D. (2003). *Geometric tools for computer graphics*. Morgan Kaufmann, San Francisco.

[Thibault and Naylor, 1987] Thibault, W. C. and Naylor, B. F. (1987). Set operations on polyhedra using binary space partitioning trees. In *Proceedings of the 14th Annual Conference on Computer Graphics and Interactive Techniques*, SIGGRAPH '87, pages 153–162, New York, NY, USA. ACM.

[Wang, 2011] Wang, C. L. (2011). Approximate boolean operations on large polyhedral solids with partial mesh reconstruction. *IEEE Transactions on Visualization and Computer Graphics*, 17(6):836–849.

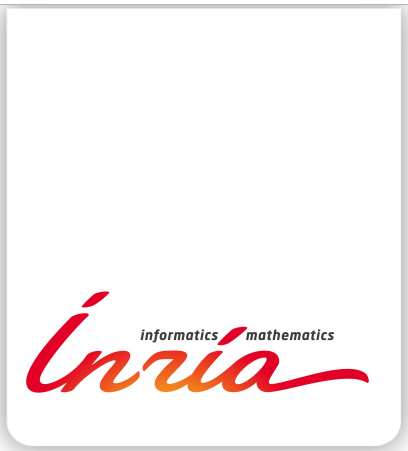

RESEARCH CENTRE
GRENOBLE – RHÔNE-ALPES

Inovallée
655 avenue de l'Europe Montbonnot
38334 Saint Ismier Cedex

Publisher
Inria
Domaine de Voluceau - Rocquencourt
BP 105 - 78153 Le Chesnay Cedex
inria.fr

ISSN 0249-6399